

Contents lists available at ScienceDirect

Petroleum Science

journal homepage: www.keaipublishing.com/en/journals/petroleum-science



Original Paper

Effects of multiphase transport in multiscale pore network on carbon storage and enhanced shale oil recovery: An experimental and numerical study



Lu Wang ^{a, b}, Gang Wu ^{c, *}, Meng Lu ^d, Xiao-Fei Fu ^a, Jun Feng ^{a, b}, Zhe-Jun Pan ^{a, b, **}

- ^a State Key Laboratory of Continental Shale Oil, Northeast Petroleum University, Daqing, 163318, Heilongjiang, China
- ^b Institute of Unconventional Oil *J* Gas, Northeast Petroleum University, Daqing, 163318, Heilongjiang, China
- ^c School of Physics and Electronic Engineering, Northeast Petroleum University, Daqing, 163318, Heilongjiang, China
- ^d CSIRO Energy, Clayton, VIC, 3169, Australia

ARTICLE INFO

Article history: Received 11 September 2024 Received in revised form 14 April 2025 Accepted 16 April 2025 Available online 16 April 2025

Edited by Yan-Hua Sun

Keywords: CO₂ sequestration Unconventional reservoirs CO₂ injection Kerogen Shale bedding fractures

ABSTRACT

CO₂ injection in shale oil reservoirs has emerged as a promising technique for simultaneously achieving CO₂ geological storage and enhancing shale oil recovery. This study investigates the potential of CO₂ injection into shale oil reservoirs with natural fractures for carbon storage and enhanced oil recovery through a combination of experimental and numerical simulations. It focuses on the synergistic effects on carbon storage capacity and oil recovery efficiency. A series of CO₂ injection experiments using online NMR T₂ and stratified T₂ technology were conducted to validate the feasibility of carbon storage and oil recovery in shale oil reservoirs. The shale samples consist of three distinct pore space systems: kerogen, inorganic matrix, and shale bedding fractures. A coupled multiscale-multiphase simulation model was developed to facilitate a comprehensive analysis of the underlying mechanisms. In the model, kerogen, inorganic matrix, and shale bedding fractures are defined as triple-continuum media. The model integrates the mechanisms of molecular diffusion, adsorption, and viscous flow to accurately represent the mass transport processes during CO2 injection in shale oil reservoirs. Within this framework, a series of mass transport partial differential equations were derived to describe the CO₂ injection process. The finite element method was used to numerically solve these equations, and the proposed model was validated against experimental results. Sensitivity analyses yielded the following results: (1) The shale bedding fractures are not only key reservoir spaces for shale oil but also the key mass transfer channels for shale oil and CO2 during CO2 injection. Increasing the permeability of the shale bedding fractures can significantly improve oil recovery efficiency and CO2 adsorption amount. (2) The kerogen content and organic porosity have a significant impact on CO2 adsorption amount and shale oil recovery factor, respectively. (3) High production pressure is essential for maximizing carbon storage capacity. Simultaneously, increasing injection pressure can effectively enhance carbon storage and shale oil recovery. © 2025 The Authors. Publishing services by Elsevier B.V. on behalf of KeAi Communications Co. Ltd. This is an open access article under the CC BY-NC-ND license (http://creativecommons.org/licenses/by-nc-nd/ 4.0/).

1. Introduction

According to the Intergovernmental Panel on Climate Change (IPCC), CO₂ can be safely stored in oil and gas reservoirs, deep saline formations, basalt, unmineable coal beds, and shale oil and gas

E-mail addresses: wugang@nepu.edu.cn (G. Wu), zhejun.pan@nepu.edu.cn (Z.-J. Pan).

reservoirs (Jin et al., 2017). The low permeability of shales effectively seals to prevent CO₂ leakage to the upper formation, and the abundance of nanoscale organic and inorganic pores, characterized by a high specific surface area, offers adequate sites for CO₂ adsorption (Lashgari et al., 2019; Wang et al., 2023). During the interaction with shale, the CO₂ can also significantly enhance shale oil recovery, improving the economic feasibility. CO₂ injection into shale oil reservoirs has emerged as a promising technology for carbon geological storage and enhanced shale oil recovery (Wang et al., 2025). Therefore, a comprehensive study for the factors impacting adsorption capacity and oil recovery potential is critical

^{*} Corresponding author.

^{**} Corresponding author.

for optimizing CO₂ injection for carbon storage and enhanced shale oil recovery.

Physical adsorption is the primary mechanism for carbon storage in shale oil reservoirs (Hazra et al., 2022; Jia et al., 2022). Many factors affect the CO₂ adsorption capacity. The gas adsorption process is exothermic. Consequently, an increase in temperature reduces the CO₂ adsorption capacity, and increasing pressure enhances CO₂ adsorption at a constant temperature (Bouzgarrou et al., 2015; Xie et al., 2021). The CO₂ adsorption capacity is positively correlated with the concentrations of organic matter and inorganic minerals, such as smectite, calcite, and illite (Aljamaan et al., 2017; Fakher and Imgam, 2019). The connected fracture network enhances the contact area with CO₂, mitigating the effects of heterogeneity and consequently increasing the carbon storage capacity (Wang et al., 2023; Martyushev et al., 2024). In addition, a previous study has confirmed the self-diffusion process of CO₂ in shale oil reservoirs using dynamic tracking technology (Fernø et al., 2015). The relative contribution of CO₂ molecular diffusion plays a vital role in low-permeability shale reservoirs, which have a significant effect on CO2 storage (Jia et al., 2019; Du and Nojabaei, 2020). Although these properties have been studied, few studies have attempted to link these properties to oil recovery in shale oil reservoirs to study the synergistic factors of carbon storage and enhanced shale oil recovery.

Shale oil reservoirs consist of organic matter (porous kerogen), inorganic matrix, and natural fractures (Yan et al., 2016). The proportion of shale oil stored in kerogen ranges from approximately 6% to 55%, with 50%-90% of this oil in an adsorbed state due to the surface properties of kerogen (Sang, 2018; Zhao et al., 2021). Kerogen exhibits a strong affinity for CO₂ due to the presence of benzene rings in its molecular structure and oxygen-containing functional groups on the graphene surface (Liu and Wilcox, 2012). CO₂ injection into shale oil reservoirs induces competitive adsorption between CO2 and oil, driven by the interactions with kerogen (Mohammed and Gadikota, 2019; Guo et al., 2024). Experimental results on the adsorption and dissolution behavior of CO₂ and *n*-alkane mixtures in shale showed that when the injected molar fraction of CO₂ reached a threshold, CO₂ could adsorb competitively and displace *n*-alkanes from kerogen. The capacity of CO₂ to displace adsorbed *n*-alkanes diminishes as the chain length of the *n*-alkanes and the temperature increase (Zhu et al., 2019). Molecular dynamics simulations of competitive adsorption between CO₂ and hydrocarbons in shale revealed that supercritical CO_2 (SC- CO_2) could mobilize adsorbed n-dodecane on the surface of silica pores. However, the distinct nano-scale surface properties of organic matter and inorganic minerals lead to a stronger adsorption affinity of CO₂ for kerogen than for inorganic minerals (Tian et al., 2019). The hydrocarbons mainly exist in the free state in inorganic pores with larger size (Zhang et al., 2015).

Among various inorganic clay minerals, the sequence of CO₂ adsorption at low pressure is calcite > illite > smectite, while at high pressure, the order shifts to smectite > calcite > illite (Tian et al., 2022). Therefore, significant differences exist between the occurrence states of shale oil and CO₂ adsorption capacity in the kerogen and inorganic matrix systems. It is essential to distinguish between these two systems. To date, the significant role of the kerogen system has received little attention in research of carbon storage and enhanced oil recovery in organic-rich shale oil reservoirs.

In this study, a series of experiments and numerical simulations were conducted to investigate the complex coupled mechanisms of carbon storage and enhanced oil recovery in multi-scale pore networks of shale oil reservoirs. Using NMR technology, the 1D T_2 and stratified T_2 techniques were applied to investigate the dynamic oil distribution and the CO_2 sweep distance during the CO_2 injection

experiments, verifying the feasibility of carbon storage and enhanced oil recovery in shale oil reservoirs. To study the fundamental mechanisms, a multiscale-multiphase numerical model was proposed. The model was characterized as triple-porosity, triple-permeability media, encompassing organic kerogen, inorganic matrix, and shale bedding fractures. The numerical model comprehensively incorporated the mechanisms of molecular diffusion, adsorption, and viscous flow of CO2 and oil in different occurrence states, indicating the mass transport processes of carbon storage and oil recovery. The finite element method was used for numerical solutions, and the simulation results were compared with experimental data to validate the numerical model. Sensitivity analyses were performed to investigate and discuss the synergistic effects of mass transfer during CO₂ injection for carbon storage and enhanced shale oil recovery. Compared with the previous works, the primary breakthroughs of this study are (1) a quantitative method for characterizing dynamic oil saturation and CO₂ sweep distance in multi-scale pores of shale oil reservoirs is developed through integrating online NMR T_2 technology and stratified T_2 technology; (2) a triple-continuum model is established based on different pore systems, the pore-scale fluid transport mechanisms are deeply analyzed; (3) a coupled multiscale-multiphase model are proposed to investigate the synergistic mechanisms of CO₂ storage and enhanced oil recovery in shale oil reservoirs.

2. Experimental methods

2.1. Materials

The shale samples were collected from the Qingshankou Formation in the Songliao Basin, China (Fig. 1). Each sample was cut parallel to the bedding surface into cylindrical cores. The physical and geochemical characteristics of the samples are listed in Table 1, including porosity, natural fracture permeability, and total organic carbon (TOC). As the total effective pore volumes of both organic and inorganic pores are accessible to non-adsorptive helium (He), which can penetrate even micropores. Therefore the porosity of the samples was measured using the gas expansion method with He (Cao et al., 2019). Natural fracture permeability was measured using the pulse decay method with He (Pan et al., 2010). The mineral compositions of the shale samples were determined through X-ray diffraction (XRD) analysis using a D8AA25 X-ray diffractometer (BRUKER, Germany), as shown in Table 2. The dominant minerals are clay minerals, quartz, plagioclase, and pyrite, with the clay mineral types primarily comprising illite/smectite interlayers, followed by illite. The density and viscosity of the light oil used in this study is 0.821 g/cm³ and 1.05 \times 10⁻² Pa·s at 25 °C, respectively. The concentration of CO₂ used in this study is 99.99%.

2.2. NMR measurements

The NMR equipment used in this study was a MacroMR12-150H-I analyzer (Guangzhou Marine Geological Survey, China). The equipment was operated at a frequency of 12 MHz, with the magnet temperature maintained at $32\pm0.02~^{\circ}$ C.

2.2.1. 1D T₂ spectrum measurement

According to the NMR phenomenon, three primary relaxation mechanisms occur in gradient magnetic fields: bulk relaxation ($T_{\rm b}$), surface relaxation ($T_{\rm s}$), and diffuse relaxation ($T_{\rm d}$), as described in Eq. (1). In natural porous rocks, $T_{\rm 2}$ relaxation for most liquids is primarily governed by surface relaxation, and the relationship between $T_{\rm 2}$ and pore size is expressed in Eq. (2) (Kleinberg and Horsfield, 1990).

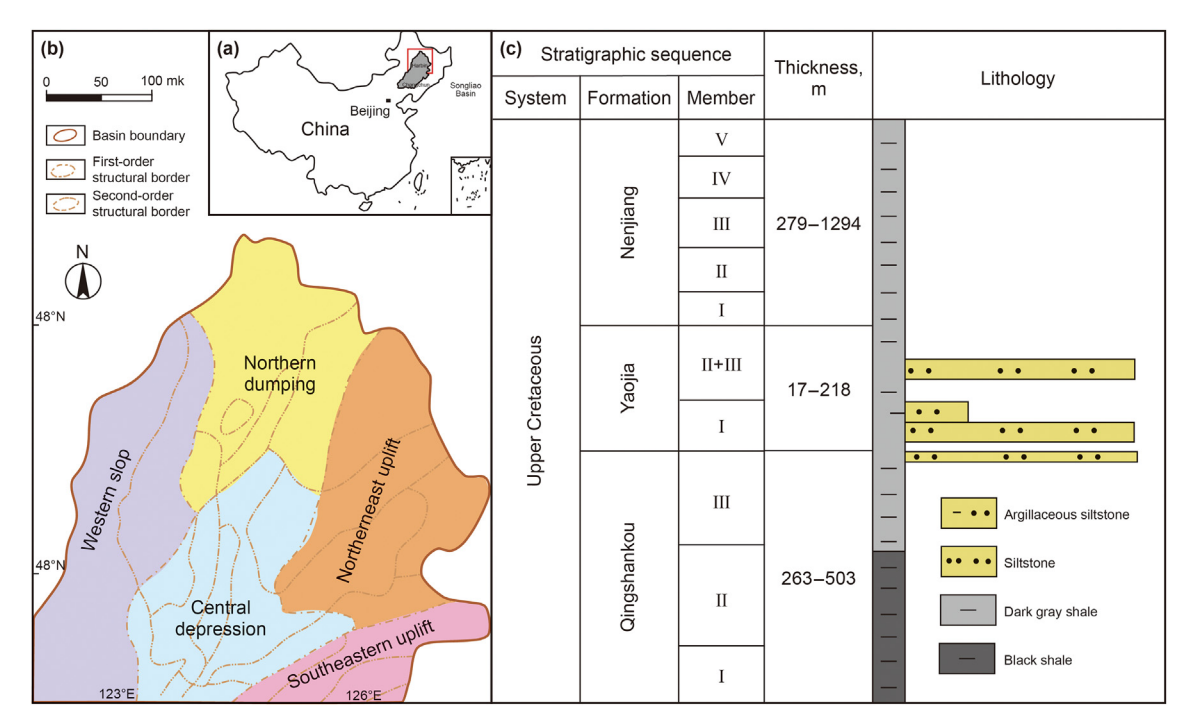


Fig. 1. Geological background of shale samples (Tian et al., 2024).

Table 1Physical and geochemical characteristics of the shale samples.

Sample	Diameter, mm	Height, mm	Depth, m	Porosity, %	Natural fracture permeability, 10^{-3} mD	TOC, wt%
Shale 1	2.54	5.05	2491.00	8.10	5.260	2.3625
Shale 2	2.50	5.12	2459.50	7.92	0.793	2.4375
Shale 3	2.49	5.01	2449.54	8.04	3.260	2.2500

Table 2 Mineral composition of the shale samples.

Sample	Mineral composition, wt%									
	Illite/smectite interlayer	Illite	Quartz	Plagioclase	Calcite	Dolomite	Pyrite	Anhydrite		
Shale 1	37.14	5.06	12.20	12.70	0	0	0.70	0		
Shale 2	53.50	3.21	13.10	21.20	0.30	0.50	2.50	0.90		
Shale 3	45.35	6.35	13.90	20.30	1.70	0	1.40	0.40		

$$\frac{1}{T_2} = \frac{1}{T_{2b}} + \frac{1}{T_{2s}} + \frac{1}{T_{2d}} \approx \frac{1}{T_{2s}}$$
 (1)

$$\frac{1}{T_2} \approx \frac{1}{T_{2s}} = \rho_2 \frac{S}{V} = \rho_2 \frac{F_s}{r}$$
 (2)

where T_{2b} is the longitudinal bulk relaxation time, s; T_{2s} is the longitudinal surface relaxation time, s; T_{2d} is the diffuse relaxation, s; ρ_2 is the longitudinal surface relaxivity, m/s; S and V are the pore surface area and volume, m²/g and m³/g, respectively; F_s is the pore morphology factors, which is 1 and 2 and 3 for planar, cylinder, and spherical pores respectively; r is the pore radius.

The quantitative oil recovery factor based on NMR can be calculated by Eq. (3).

$$E_{R} = \frac{S_{oi} - S_{of}}{S_{oi}} = \frac{\int_{r_{2}}^{T_{r_{1}}} \left(A_{i} - A_{f}\right) dT}{\int_{T_{r_{1}}}^{T_{r_{1}}} A_{i} dT} \times 100\%$$
(3)

where E_R is the oil recovery factor; S_{oi} is the oil saturation of core before oil displacement; S_{of} is the oil saturation of core after oil displacement; T_{r_1} and T_{r_2} are the T_2 values of the pore with radius of r_1 and r_2 , respectively, ms; A_i and A_f are the NMR signal areas before and after gas injection, respectively.

The 1D T_2 spectra were obtained using the CPMG sequence. The NMR T_2 spectrum is utilized to characterize the coupled information of oil recovery factor and pore size distribution (Yao et al.,

Table 3 Parameters of CMPG and SFG-MSCPMG sequence in this study.

Sequence	Frequency, MHz	Frequency offset, Hz	90° pulse length, μs	180° pulse length, μs	Waiting time, ms	Number of superimposed signals	Echo time, ms	Number of echoes
CPMG	12	411068.91	21	35.04	3000	32	8000	0.12
SFG-	12	411068.91	21	35.04	5000	32	5000	0.12
MSCPMG								

2010; Li et al., 2017; Ge et al., 2021). The parameters of the CMPG sequence were listed in Table 3.

2.2.2. Stratified T₂ measurement

The stratified T_2 technique can be used to characterize the spatial resolution of the T_2 distribution and to monitor CO_2 sweep distance (Luo et al., 2022; Q. Liu et al., 2023). Due to it is not constrained by gradient encoding, the SFG-MSCPMG sequence enables the measurement of a greater number of short relaxation signals, making it suitable for accurately measuring shale samples with short relaxation times and low signal intensity. In this study, the core sample was uniformly segmented into five layers along the axial direction, each with a thickness of 1 ± 0.05 cm, as shown in Fig. 2. The parameter settings for the SFG-MSCPMG sequence are listed in Table 3.

2.3. SEM and N_2 adsorption measurements

Argon ion milling combined with field emission scanning electron microscopy (FE-SEM) can be employed to observe the pore types, sizes, and numbers of micropores and microfractures in the shale samples (Gou et al., 2019). SEM images are acquired using the Zeiss-Merlin compact system with an accelerating voltage of 2 kV. A maximum pixel resolution of approximately 4 nm can be achieved at an acceleration voltage of 10 kV (Cao et al., 2019). Organic pores, inorganic pores, and micro-fractures in the shale samples are identified based on SEM images (Zhao et al., 2022).

The pore structures of micropores and mesopores in the shale samples are characterized by the low-temperature N_2 isothermal adsorption method (Cao et al., 2019). Low-pressure N_2 adsorption and desorption measurements are conducted at 77 K. The specific surface area is calculated using the BET model. The pore volume and PSD of the shale samples are determined using the BJH model. The measurable pore size range is 1.2–100 nm (Gao et al., 2023).

2.4. Experimental apparatus and procedures

The CO₂ injection apparatus used in this study, based on an online NMR technique, consisted of five modules: a fluid injection module, a high-temperature and high-pressure circulation module, a core holder module, a NMR measurement module, and a fluid production module, as illustrated in Fig. 3. The fluid injection

module included a CO_2 tank, a constant-pressure pump with flow control, a flowmeter, and a heater for pressure regulation. The high-temperature and high-pressure circulation module was used to apply confining pressure and control temperature. The maximum confining pressure and temperature achievable were 40 MPa and $100\,^{\circ}\text{C}$, respectively. The core holder was used to load cores, isolate the confining fluid, and introduce the displacement media. The NMR measurement module utilized a MacroMR12-150H-1 analyzer (Guangzhou Marine Geological Survey, China). The fluid production module comprised backpressure devices and gas flow measurement instruments.

All shale samples were prepared and tested using the same procedure to ensure consistent comparison of results. The experimental procedure for CO_2 injection experiments is shown as follows:

Preparation process: (a) Clean the as-received cores of any residual saline water and oil. (b) Dry the samples under 120 °C until a constant weight is achieved.

Saturation process: (a) Immerse the shale core in the saturation vessel. (b) Apply vacuum (-0.1 MPa) followed by high pressure (30 MPa) for oil saturation until the weight and $1D T_2$ distribution of the samples remain constant.

CO₂ injection process: (a) For gaseous CO₂ injection, CO₂ was sequentially injected into the core at constant pressures of 1, 3, and 5 MPa, with the back pressure at the outlet set to atmospheric pressure. (b) For the SC-CO₂ injection, SC-CO₂ was sequentially injected into the core at constant pressures of 9, 11, and 13 MPa, with the back pressure set to 8 MPa.

During both gaseous CO_2 and $SC-CO_2$ injection stages, the confining pressure was consistently maintained 3 MPa higher than the injection pressure. Each pressure stage of the experiment was terminated when gas breakthrough occurred at the outlet. Following each repetition of the saturation operation, the subsequent injection pressure experiment was conducted until all designated pressures were tested. The experimental temperature was maintained at a constant 35 $^{\circ}C$.

3. Experimental results

3.1. Full-scale pore structure characteristics

SEM, low-pressure N2 adsorption, and NMR methods were

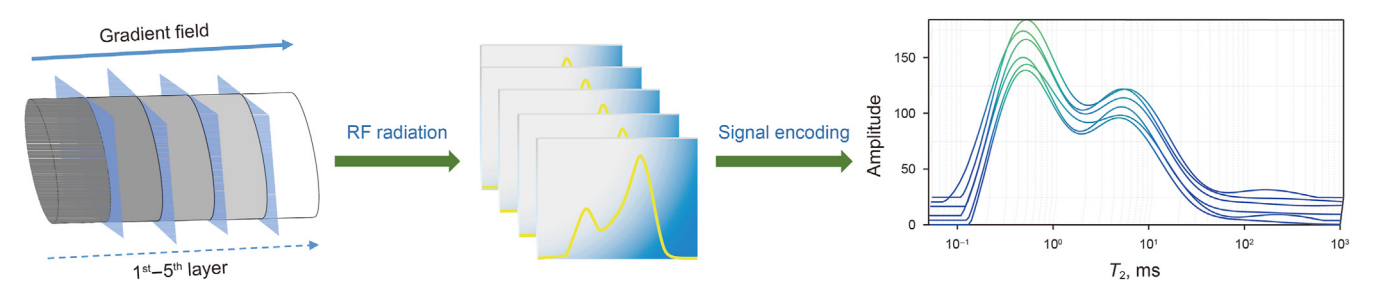


Fig. 2. The schematic diagram of the stratified T_2 measuring process.

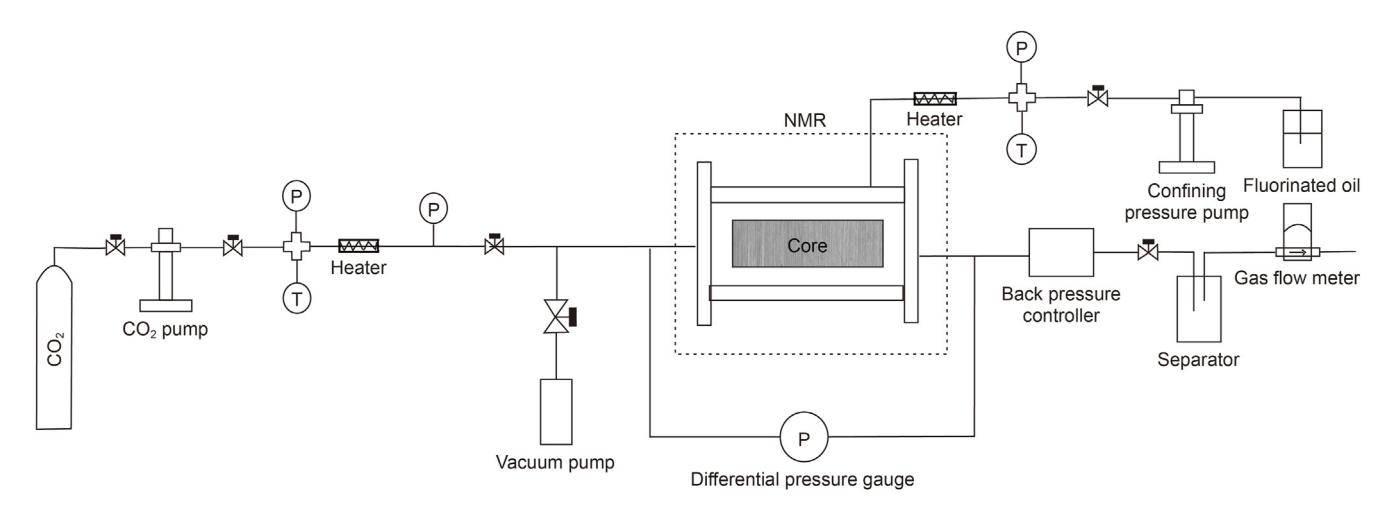


Fig. 3. The diagram of CO₂ injection apparatus based on an online NMR technique.

comprehensively applied to characterize the multi-scale pore structures of the shale samples (Fu et al., 2023; Zhao et al., 2024).

SEM images of the shale samples showed the development of various types of pore space, including inorganic pores, organic pores, and shale bedding fractures (Fig. 4). The pore sizes of both inorganic and organic pores ranged from several nanometers to several hundred nanometers. Inorganic pore types included interparticle (interP) and intraparticle (intraP) pores, with interparticle (interP) pores being the main type. Organic pores were primarily developed in kerogen, predominantly exhibiting sub-

circular shapes. Additionally, SEM images showed that numerous bedding fractures, ranging from 1 to 10 μ m in width, were densely distributed in the shale samples (Fig. 4(c) and (d)).

The PSD curves from N_2 adsorption were calculated using the BJH model (Hu et al., 2015). The cumulative surface areas of the shale 1, shale 2, and shale 3 were measured as 14.582, 13.393, and 13.637 m²/g, respectively. The pore volumes were 0.0252, 0.0269, and 0.0258 cm³/g, respectively. The average pore diameters were 6.905, 8.046, and 7.560 nm, respectively, indicating that the shale samples primarily consist of micropores. The N_2 adsorption PSD



Fig. 4. Pore types in the shale samples observed by SEM images. (a) and (b) are view fields of the shale matrix; (c) and (d) are view fields of the shale bedding fractures.

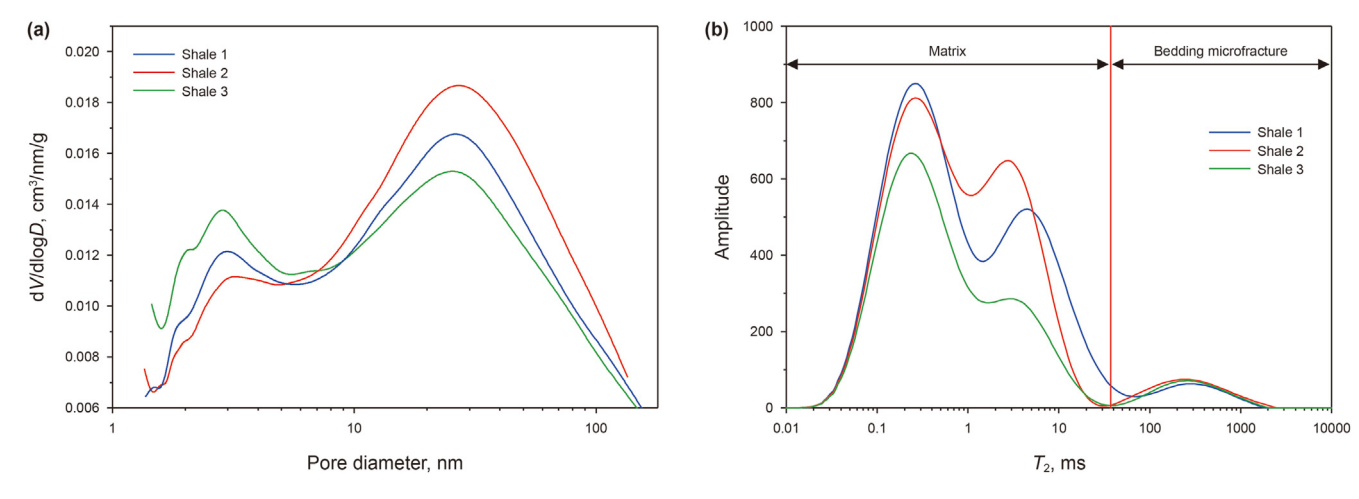


Fig. 5. Pore size distribution results of N_2 adsorption (a) and NMR T_2 spectrum (b).

curves showed bimodal peaks, as illustrated in Fig. 5(a). As the N_2 adsorption method is effective only for measuring pores smaller than 100 nm, it is unable to capture the $\mu m\text{-scale}$ shale bedding fractures observed in SEM images.

1D NMR T_2 spectrum is an effective technique for characterizing the full-scale PSD of shale. To mitigate the influence of kerogen and clay-bound water signals, the T_2 signal of the dried sample was subtracted from the T_2 spectrum of the fully saturated fluid sample, providing the foundation for PSD analysis (Yao et al., 2010; Fu et al., 2024). The NMR T_2 distributions of the shale samples exhibited displayed three distinct peaks, indicating the multi-scale pore structure. The two left peaks of the T_2 spectrum were consistent with the bimodal distribution of nanopores observed in T_2 adsorption measurements. Due to the positive correlation between T_2 relaxation times and pore diameters, the right peak of the T_2 spectrum represented pore spaces corresponding to the micrometer-scale bedding fractures identified by SEM analysis, as illustrated in Fig. 5(b).

3.2. Oil distribution in multi-scale pore system during CO₂ injection

The cumulative recovery factors for the three samples were determined using the NMR T_2 map (Fig. 6). The results demonstrated that, under the same injection pressure, the cumulative recovery factors for SC-CO₂ injection were higher than those of gaseous CO₂ injection. Under the same pressure, the cumulative oil recovery factor of the different samples was positively correlated with the bedding fracture permeability, indicating that the shale bedding fractures are the main channels for CO₂ and oil transport.

The stratified T_2 technique enhances spatial resolution, enabling more detailed characterization of oil distribution dynamics in multi-pore systems within the CO_2 sweep distance (Luo et al., 2022; Lv et al., 2024). The variations in NMR T_2 distributions across different spatial layers of shale 1 reflected the strong heterogeneity. These results indicated that within the sweep area, SC- CO_2 effectively diffused into the matrix during injection, displacing oil into the bedding fractures, as shown in Fig. 7. The higher injection pressure during SC- CO_2 injection expanded the CO_2 sweep area within the shale matrix, leading to a higher oil recovery factor, contributing to the higher cumulative recovery factor observed for SC- CO_2 compared to gaseous CO_2 .

Although experimental results provided pore-scale insight into oil distribution in the shale matrix and bedding fractures during CO_2 injection, the volume of CO_2 that diffusing into the matrix and the amount of CO_2 adsorbed in multiple pore systems under

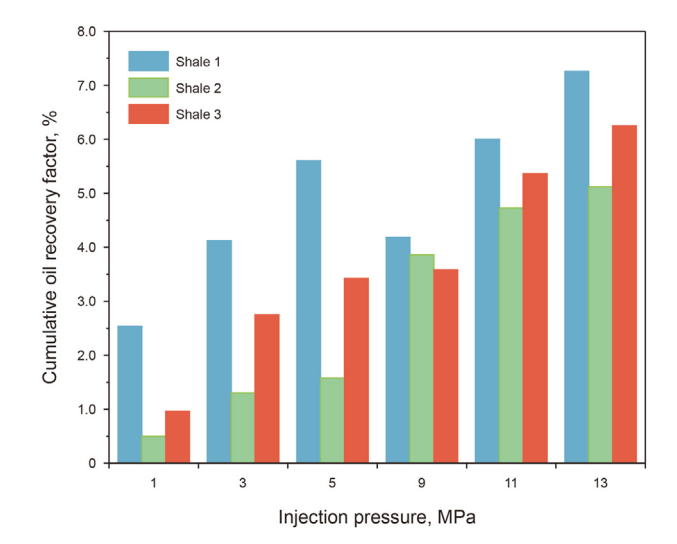


Fig. 6. The cumulative recovery factors for three samples under different injection pressures.

varying oil saturation were difficult to determine experimentally. To address this issue, a multi-scale and multi-phase numerical model was developed to better understand the mass transfer mechanisms, incorporating molecular diffusion, adsorption, and viscous flow effects of oil and CO₂ phases in shale oil reservoirs.

4. Methodology

4.1. Physical model

A fully coupled multi-scale and multi-phase model was developed to account for the complex mechanisms involved in CO₂ injection in shale oil reservoirs. The kerogen system, inorganic matrix system, and shale bedding fracture system were defined as triple-porosity and triple-permeability media, as depicted in Fig. 8.

As demonstrated in Section 3.2, the shale bedding fractures are the main channels for CO_2 and oil transfer (Y. Liu et al., 2023). The shale bedding fractures exhibit higher porosity and permeability, in which oil and CO_2 flow mainly follow continuous flow governed by Darcy's law (Martyushev et al., 2023; Zhao et al., 2023).

The shale matrix consists of inorganic matrix and organic kerogen system (Sun et al., 2022). The mineral composition of the

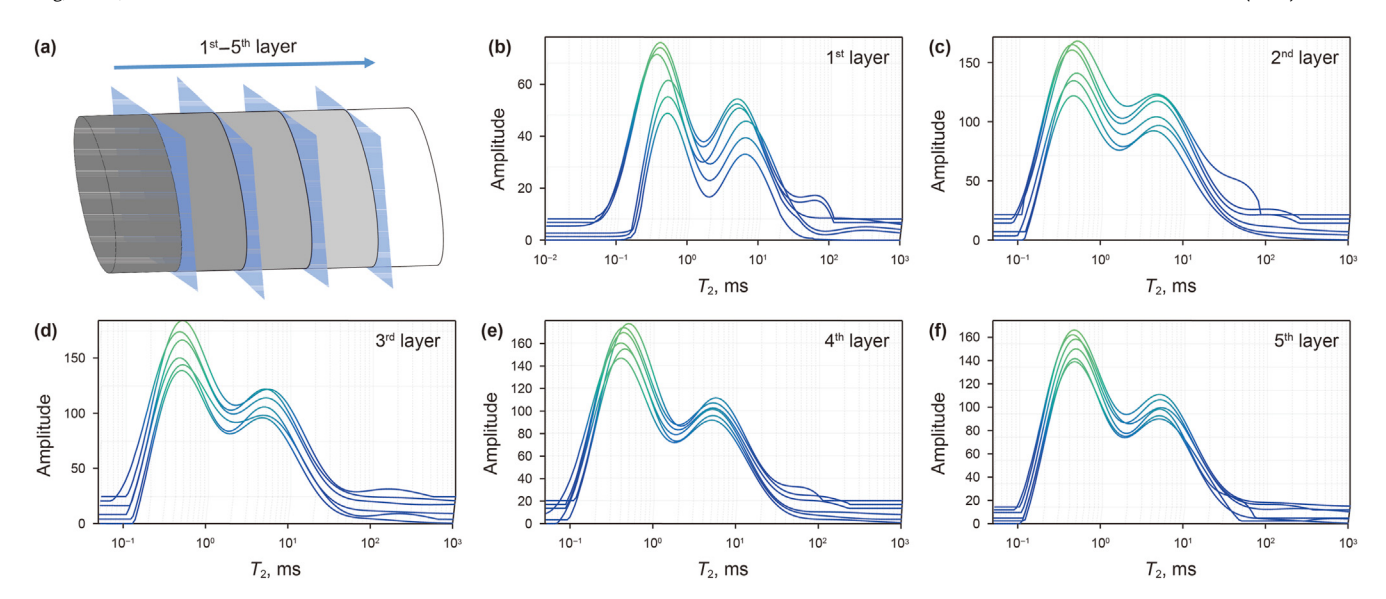


Fig. 7. The spatial T_2 curves of shale 1 under different injection pressures. Notes: T_2 distribution curves in (**b**)–(**f**) from far to near the reader are at the CO₂ injection pressure of 1, 3, 5, 9, 11, and 13 MPa, in sequence.

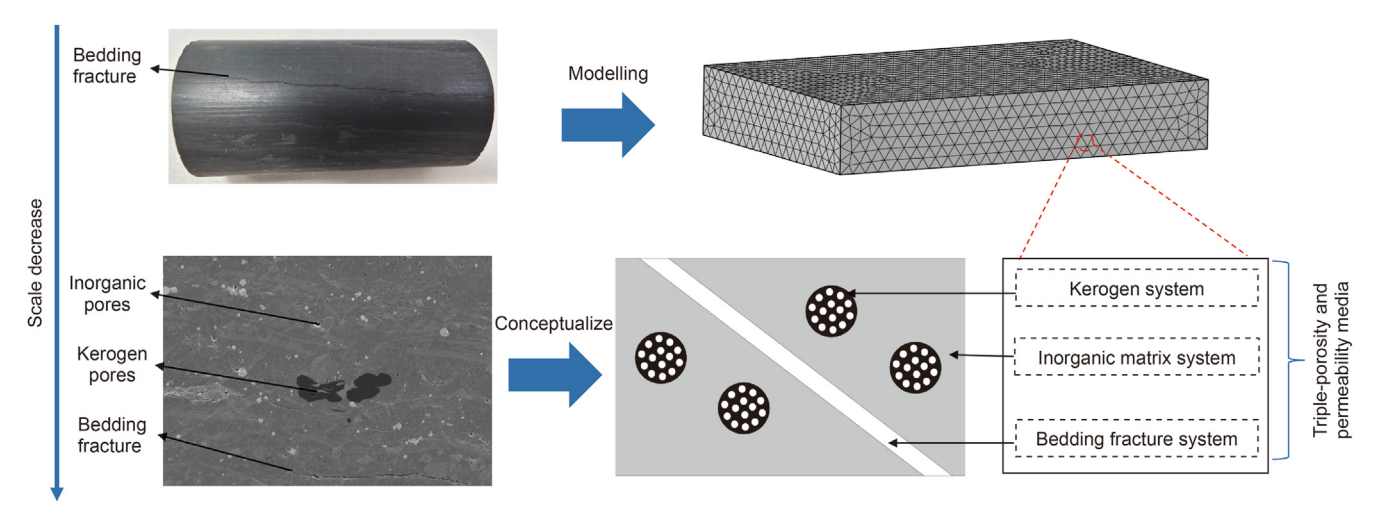


Fig. 8. Conceptual triple-continuum model for shale oil reservoir.

inorganic matrix primarily includes clay minerals, quartz, and feldspar. Oil within the inorganic pore space is typically present in a free state (Xu et al., 2024). CO₂ penetrates the inorganic matrix system through diffusion and flow, displacing oil from the pores and adsorbing onto the mineral surfaces, thereby contributing to carbon storage. In the kerogen system, owing to its lipophilicity, oil exists in both free and adsorbed states (Falk et al., 2015; Zhao et al., 2021; Zhao and Zhou, 2024). CO₂ infiltration into kerogen can disrupt the equilibrium between adsorbed and free oil, leading to the desorption of oil from the kerogen surface (Sang, 2018). The strong affinity of kerogen for CO₂ facilitates the physical adsorption of CO₂ within the kerogen system (Zhu et al., 2018b; Sui et al., 2023). The organic pores in kerogen form an interconnected pore network through particle contact, enabling oil to flow from the kerogen into the inorganic matrix.

4.2. Mathematical model and solution

4.2.1. Assumptions

The following are the assumptions for the proposed model:

- The organic kerogen, inorganic pores, and shale bedding fractures are considered as uniformly distributed continuum.
- (2) The thickness of the adsorption phase is assumed negligible.
- (3) Shale bedding fractures are simplified as horizontal fracture media.

The shale bedding fractures, organic pores, and inorganic pores within the unfractured shales are dispersed, as indicated by SEM images (Fig. 4). Nanometer to micrometer fractures are the connected pathways between the shale matrix and the shale bedding fractures. Therefore, in Assumption 1, the multi-scale porous space is modeled as a uniformly distributed continuum.

Assumption 2 is widely accepted in adsorption theory due to the thickness of the adsorption phase is generally much smaller than the pore diameter (Javadpour et al., 2007; Yang et al., 2016; Zhu et al., 2018b).

Shale samples are cut along the horizontal bedding direction, with CO_2 injection aligned to the bedding fracture direction. Therefore, the bedding fracture system is simplified as horizontally oriented in Assumption 3.

4.2.2. Mass transfer model for kerogen

The mass transfer mechanisms in the numerical model include molecular diffusion, adsorption, and viscous flow of oil and CO₂ phases in the proposed numerical model, as illustrated in Fig. 9.

The mathematical model is described as follows.

4.2.2.1. Oil mass transport in kerogen

Due to the uncertainties and diversities of matrix geometry, the shape factor is obtained from history match and can be described as (Kazemi et al., 1976)

$$\alpha = 4 \left(\frac{1}{L_{f,x}^2} + \frac{1}{L_{f,y}^2} + \frac{1}{L_{f,z}^2} \right) \tag{6}$$

The density of free oil in kerogen is described as

$$\frac{\partial}{\partial t} \left(\varepsilon_{kp} \rho_o^k \phi_m S_o^k + \varepsilon_{ks} \left(1 - \phi_m - \phi_f \right) \rho_{ado}^k \right) + \nabla \cdot \left(- \frac{\rho_o^k K_{ro}^k K_k}{\mu_o} \nabla P_o^k \right) = -q_o^{ki}$$

$$\tag{4}$$

where the subscript k refers to the kerogen system; the subscript f refers to the shale bedding fracture system; the subscript o refers to the oil; $\varepsilon_{\rm kp}$ is the volume fraction of organic pores; $\phi_{\rm m}$ and $\phi_{\rm f}$ represent the porosity of the shale matrix and bedding fractures, respectively; $S_{\rm o}^{\rm k}$ is the oil saturation in kerogen system; $\varepsilon_{\rm ks}$ is the volume fraction of organic kerogen; $\varepsilon_{\rm ks}(1-\phi_{\rm m}-\phi_{\rm f})$ is the kerogen solid volume per unit bulk volume of shale; $K_{\rm k}$ represents the apparent permeability of organic kerogen, ${\rm m}^2$; $K_{\rm ro}^{\rm k}$ is the relative permeability of oil in the kerogen system; $\rho_{\rm o}^{\rm k}$ is the oil density in the kerogen system, kg/m³; $\mu_{\rm o}$ is the oil viscosity, Pa·s; $P_{\rm o}^{\rm k}$ is the pressure in kerogen, MPa; $q_{\rm o}^{\rm ki}$ represents the oil flow rate between the kerogen system and the inorganic system, kg/(m³·s).

According to the Warren-Root PSS transfer model, q_0^{ki} is defined as (Warren and Root, 1963)

$$q_{o}^{ki} = S_{o}^{k} \frac{\alpha K_{k} K_{ro}^{k} \rho_{o}^{k}}{\mu_{o}} \left(P_{o}^{k} - P_{o}^{i} \right)$$
 (5)

where α is the shape factor, $1/m^2$.

$$\rho_{o}^{k} = \rho_{o}^{in} e^{C_{o} \left(P_{o}^{k} - P_{o}^{in}\right)} = \rho_{o}^{in} \left[1 + C_{o} \left(P_{o}^{k} - P_{o}^{in}\right) \right]$$
 (7)

where ρ_0^{in} is the initial density of oil, kg/m³; C_0 is the oil compressibility, 1/Pa.

The density of adsorbed oil in kerogen system is described as (Langmuir, 1918)

$$\rho_{\text{ado}}^{k} = \rho_{\text{oatm}} \rho_{km} \frac{V_{\text{Lo}}^{k} P_{\text{O}}^{k}}{P_{\text{O}}^{k} + P_{\text{Lo}}^{k}}$$

$$\tag{8}$$

where $\rho_{\rm oatm}$ is the oil density at atmospheric pressure, kg/m³; $\rho_{\rm km}$ is the density of kerogen, kg/m³; $V_{\rm Lo}^k$ is the Langmuir volume of oil in kerogen, which shows the maximum adsorbed volume converted into the standard condition (273.15 K and 101.325 kPa) per unit total grain mass, m³/kg; $P_{\rm Lo}^k$ denotes the Langmuir pressure constant of oil in kerogen system, MPa.

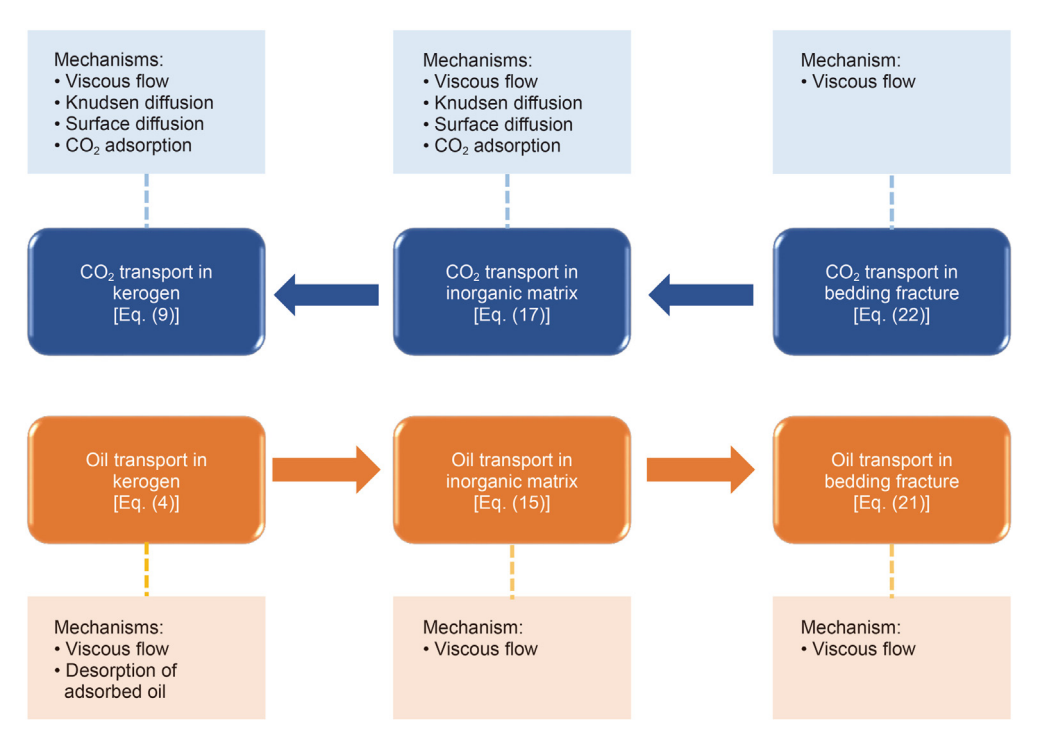


Fig. 9. The flowchart of the numerical simulation model for the shale oil reservoir.

4.2.2.2. CO₂ mass transport in kerogen

$$\frac{\partial}{\partial t} \left(\varepsilon_{kp} \phi_m c_g^k S_g^k + \varepsilon_{ks} \left(1 - \phi_m - \phi_f \right) c_{adg}^k \right) - \nabla \cdot \left(\frac{c_g^k K_k K_{rg}^k}{\mu_g} \right) \nabla P_g^k - \nabla \cdot \left(\varepsilon_{kp} \phi_m D_k^k c_g^k \right) - \nabla \cdot \left[\varepsilon_{ks} \left(1 - \phi_m - \phi_f \right) D_s^k c_g^k \right] = q_g^{ik} / M_g \tag{9}$$

where the subscript g refers to the CO₂ in the kerogen system; $c_{\rm g}^{\rm k}$ is the concentration of CO₂ in the kerogen system, mol/m³; $P_{\rm g}^{\rm k}$ is the pressure of CO₂ in the kerogen system; $\mu_{\rm g}$ is the viscosity of CO₂, Pa·s; $M_{\rm g}$ is the molar mass of CO₂, kg/mol.

The equation of state to describe the concentration of CO_2 in the kerogen system is

$$c_g^k = \frac{1}{RT} P_g^k \tag{10}$$

According to the Warren-Root PSS transfer model, the interflow rate of CO₂ between the inorganic matrix system and kerogen system is defined as (Warren and Root, 1963)

$$q_{\rm g}^{\rm ik} = S_{\rm g}^{\rm i} \frac{\alpha K_{\rm i} K_{\rm rg}^{\rm i} \rho_{\rm g}^{\rm k}}{\mu_{\rm g}} \left(P_{\rm g}^{\rm i} - P_{\rm g}^{\rm k} \right) \tag{11}$$

where $S_{\rm g}^{\rm i}$ is the saturation of ${\rm CO_2}$ in the inorganic matrix system; $K_{\rm rg}^{\rm i}$ is the relative permeability of ${\rm CO_2}$ in the inorganic matrix system; $P_{\rm g}^{\rm i}$ is the ${\rm CO_2}$ pressure in the inorganic matrix system.

The gas transport in nanopores can be driven by pressure difference, Knudsen diffusion and surface diffusion in kerogen system.

The effective Knudsen diffusivity can be expressed as (Cao et al., 2017)

$$D_{\mathbf{k}}^{\mathbf{k}} = \frac{\phi_{\mathbf{k}}}{\tau_{\mathbf{k}}} \frac{2r_{\mathbf{k}}}{3} \sqrt{\frac{8RT}{\pi M_{\mathbf{g}}}} \tag{12}$$

where τ_k is the tortuosity of kerogen.

 CO_2 is adsorbed on the kerogen surface due to the strong affinity (Wei et al., 2016). The surface diffusion of CO_2 in the kerogen is expressed as (Zhang et al., 2015)

$$D_{s}^{k} = \frac{N_{ks}}{-\varepsilon_{ks} \left(1 - \phi_{m} - \phi_{f}\right) \nabla \cdot c_{\mu}}$$
(13)

$$c_{\text{adg}}^{k} = \frac{\rho_{\text{gatm}} \rho_{k}}{M_{g}} \frac{V_{\text{Lg}}^{k} P_{g}^{k}}{P_{g}^{k} + P_{\text{Lg}}^{k}}$$
(14)

where $\rho_{\rm gatm}$ is the CO₂ density at atmospheric pressure; $\rho_{\rm k}$ is the density of kerogen, kg/m³; $V_{\rm Lg}^{\rm k}$ is the Langmuir volume of CO₂ in the kerogen system, which shows the maximum adsorbed gas volume converted into the standard condition (273.15 K and 101.325 kPa) per unit total grain mass, m³/kg; $M_{\rm g}$ is the molar mass of CO₂, kg/mole; $P_{\rm Lg}^{\rm k}$ denotes the Langmuir pressure constant of CO₂ in the kerogen system, MPa. The corresponding Langmuir parameters is obtained from the literature (Huang et al., 2018).

4.2.3. Mass transfer model for inorganic matrix 4.2.3.1. Oil mass transport in IM

$$\frac{\partial}{\partial t} \left(\left(1 - \varepsilon_{\mathbf{kp}} \right) \phi_{\mathbf{m}} \rho_{\mathbf{o}}^{\mathbf{i}} S_{\mathbf{o}}^{\mathbf{i}} \right) - \nabla \cdot \left(\frac{K_{\mathbf{i}} K_{\mathbf{ro}}^{\mathbf{i}} \rho_{\mathbf{o}}^{\mathbf{i}}}{\mu_{\mathbf{o}}} \right) \nabla P_{\mathbf{o}}^{\mathbf{i}} = q_{\mathbf{o}}^{\mathbf{ki}} - q_{\mathbf{o}}^{\mathbf{if}}$$
(15)

where the subscript "i" refers to the inorganic matrix system; $\phi_{\rm m}$ is the porosity of the shale matrix, including kerogen and inorganic matrix; $\rho_{\rm o}^{\rm i}$ is the oil density in the inorganic system, kg/m³; $S_{\rm o}^{\rm i}$ is the oil saturation in the inorganic system; $K_{\rm i}$ represents the apparent permeability of inorganic matrix, m²; $K_{\rm ro}^{\rm i}$ is the relative permeability of oil in inorganic matrix system; $P_{\rm o}^{\rm i}$ is the pressure in the inorganic matrix system, MPa; $P_{\rm o}^{\rm f}$ is the pressure in shale bedding fracture system, MPa.

The inter flow rate of oil between the bedding fracture system and inorganic system is defined as (Warren and Root, 1963):

$$q_o^{if} = S_o^i \frac{\alpha K_i K_{ro}^i \rho_o^i}{\mu_o} \left(P_o^i - P_o^f \right)$$
 (16)

4.2.3.2. CO₂ mass transport in IM

$$\frac{\partial}{\partial t} \left(\left(1 - \varepsilon_{kp} \right) \phi_{m} c_{g}^{i} S_{g}^{i} + \varepsilon_{is} \left(1 - \phi_{m} - \phi_{f} \right) c_{adg}^{i} \right) - \nabla \cdot \left(\frac{K_{i} K_{rg}^{i} c_{g}^{i}}{\mu_{g}} \right) \nabla P_{g}^{i} - \nabla \cdot \left(\left(1 - \varepsilon_{kp} \right) \phi_{m} D_{g}^{i} c_{g}^{i} \right) - \nabla \cdot \left(\varepsilon_{is} \left(1 - \phi_{m} - \phi_{f} \right) D_{s}^{i} c_{ads}^{i} \right) \\
= \left(q_{g}^{fi} - q_{g}^{ik} \right) / M_{g} \tag{17}$$

The concentration of adsorbed CO₂ in the kerogen system is described as

where ε_{is} is the portion of inorganic solid volume; $\varepsilon_{is}(1-\phi_m-\phi_f)$ is the inorganic matrix solid volume per unit bulk volume.

The equation of state to describe the concentration of CO₂ in inorganic matrix system is written as

$$c_{\rm g}^{\rm i} = \frac{1}{RT} P_{\rm g}^{\rm i} \tag{18}$$

The density of adsorbed CO₂ in inorganic matrix system is described based on Langmuir model:

$$c_{\text{adg}}^{i} = \frac{\rho_{\text{gatm}} \rho_{\text{im}}}{M_{g}} \frac{V_{\text{Lg}}^{i} P_{g}^{i}}{P_{g}^{i} + P_{\text{Lg}}^{i}}$$
(19)

where ρ_{im} is the density of inorganic matrix, kg/m³; V_{Lg}^{i} is the Langmuir volume of CO_2 in inorganic matrix system, m^3/kg ; P_g^i is the pressure of CO_2 in inorganic matrix system, MPa; P_{Lg}^i denotes the Langmuir pressure constant of CO_2 in inorganic matrix system, MPa. The corresponding Langmuir parameters were obtained from the literature (Chouikhi et al., 2019).

The inter flow rate of CO₂ between the inorganic matrix and the shale bedding fracture systems is written as

$$q_{\rm g}^{\rm fi} = S_{\rm g}^{\rm f} \frac{\alpha K_{\rm f} K_{\rm fg}^{\rm f} \rho_{\rm g}^{\rm f}}{\mu_{\rm g}} \left(P_{\rm g}^{\rm f} - P_{\rm g}^{\rm i} \right) \tag{20}$$

4.2.4. Mass transfer model for shale bedding fracture system

4.2.4.1. Oil mass transport in BF

$$\frac{\partial}{\partial t} \left(\phi_{\rm f} \rho_{\rm o}^{\rm f} S_{\rm o}^{\rm f} \right) - \nabla \cdot \left(\frac{K_{\rm f} K_{\rm ro}^{\rm f} \rho_{\rm o}^{\rm f}}{\mu_{\rm o}} \right) \nabla P_{\rm o}^{\rm f} = q_{\rm o}^{\rm if} \tag{21}$$

where ρ_0^f the oil density of in shale bedding fracture system, kg/m³; $S_0^{\rm f}$ is the oil saturation in shale bedding fracture system.

4.2.4.2. CO₂ mass transport in BF

$$\frac{\partial}{\partial t} \left(\phi_f \rho_g^f S_g^f \right) - \nabla \cdot \left(\frac{K_f K_{fg}^f \rho_g^f}{\mu_g} \right) \nabla P_g^f = - q_g^{fi} \tag{22} \label{eq:22}$$

According to the equation of state, the CO₂ density is described

$$\rho_{\rm g}^{\rm f} = \frac{M_{\rm g}}{RT} P_{\rm g}^{\rm f} \tag{23}$$

4.3. Initial and boundary conditions

4.3.1. Initial condition

$$P_{\mathbf{g}}^{\mathbf{f}}(x,y,t)\Big|_{t=0} = P_{\mathbf{atm}} \tag{24}$$

$$P_{g}^{i}(x,y,t)\Big|_{t=0} = P_{atm}$$
 (25) $S_{e} = \frac{S_{0} - S_{or}}{1 - S_{or}}$

 $P_{\rm c} = P_{\rm e} S_{\rm e}^{-\frac{1}{\lambda}}$

$$P_{g}^{k}(x,y,t)\Big|_{t=0} = P_{atm}$$

$$K_{ro} = S_{e}^{\frac{2+3\lambda}{\lambda}}$$

$$(26) \qquad K_{ro} = S_{e}^{\frac{2+3\lambda}{\lambda}}$$

$$S_0^f(x, y, t)\Big|_{t=0} = 1$$
 (27)

$$S_0^i(x, y, t)\Big|_{t=0} = 1$$
 (28)

$$S_0^k(x, y, t)\Big|_{t=0} = 1$$
 (29)

where P_{atm} is the atmospheric pressure, which is approximately 0.1 MPa.

4.3.2. Boundary condition

$$P_{\mathbf{g}}^{\mathbf{f}}(x,y,t)\Big|_{t=0} = P_{\mathbf{i}\mathbf{n}} \tag{30}$$

$$P_{\mathbf{g}}^{\mathbf{f}}(x,y,t)\Big|_{\mathbf{x}=\mathbf{I}} = P_{\text{out}} \tag{31}$$

$$\frac{\partial P_{g}^{k}}{\partial n} \left| \Gamma = \frac{\partial P_{g}^{i}}{\partial n} \right| \Gamma = 0$$
(32)

$$\left. \frac{\partial P_{\rm g}^{\rm f}}{\partial n} \right| \Gamma_{\rm X} = 0 \tag{33}$$

$$S_0^f \Big|_{\mathbf{x} = I} = 1 \tag{34}$$

$$\frac{\partial S_0^f}{\partial n} \left| \Gamma_X = \frac{\partial S_0^f}{\partial n} \right|_{x=0} = 0 \tag{35}$$

$$\frac{\partial S_o^i}{\partial n} \left| \Gamma = \frac{\partial S_o^k}{\partial n} \right| \Gamma = 0 \tag{36}$$

where Γ is the total boundary of the shale core 2D model; Γ_x is the boundary in the x direction, which is parallel to the injection direction; n is the normal direction of the outer boundary; P_{in} is the CO₂ injection pressure, MPa; Pout is the back pressure at the outlet, MPa.

4.4. Constraint equations

Constraint conditions are provided below for solving the partial differential equations.

$$P_{\rm c} = P_{\rm g} - P_{\rm o} \tag{37}$$

$$S_0 + S_g = 1 \tag{38}$$

(39)

$$K_{\rm ro} = S_{\rm e}^{\frac{2+3\lambda}{\lambda}} \tag{43}$$

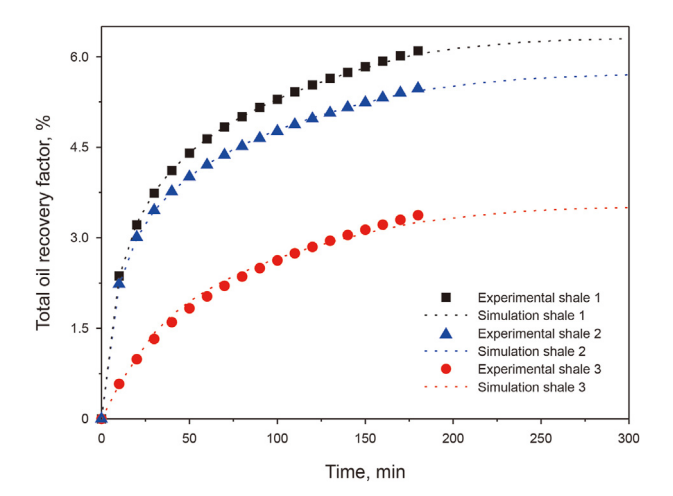


Fig. 10. Comparison of the numerical simulation results of the proposed model with the experimental oil recovery results.

$$K_{\rm rg} = (1 - S_{\rm e})^2 \left(1 - S_{\rm e}^{\frac{2+\lambda}{\lambda}}\right)$$
 (42)

where S_e is the effective oil saturation; P_e is the non-wetting phase entry pressure, MPa; λ is related to the pore size distribution:

materials with smaller variations in pore size have a larger λ value. Usually, 0. $2 \le \lambda \le 3$ (Reichenberger et al., 2006); $S_{\rm or}$ is the irreducible oil saturation; $K_{\rm ro}$ and $K_{\rm rg}$ are respectively the relative permeabilities of oil and gas; $P_{\rm c}$ is the capillary pressure, MPa.

4.5. Model solution

The unstructured grid method is used in this study to discretize the nonlinear control equations, subdividing the shale core into three-dimensional (3D) triangular prisms (Fig. 8). The implicit numerical model is solved using Newton—Raphson iteration to ensure a stable solution (Zhang et al., 2021). The saturation levels of $\rm CO_2$ and oil are computed via finite element analysis. For simplification, the model is reduced to a two-dimensional (2D) rectangle, where the *x*-axis represents the length of core, and the *y*-axis corresponds to the thickness of the lamination. The mesh elements for both the free and absorption phases range in size from 0.00375 to 1 mm. The simulation time spans from 0 to 6 h, with increments of at steps of 0.5 h.

4.6. Model verification

The experimental results, obtained using the online NMR technique for the cumulative oil recovery of the three shale samples during SC-CO₂ injection under 11 MPa are utilized to validate the proposed model. A comparison between experimental data and numerical simulation results is shown in Fig. 10. Parameters of the

Table 4 Parameter estimation results for shale samples.

Sample	λ	K _k , mD	K _i , mD	S_{or}	$arepsilon_{ m kp}$	$arepsilon_{ ext{ks}}$	$arepsilon_{ ext{is}}$	$\phi_{ m m}$	$\phi_{ m f}$
Shale 1 Shale 2	0.8 1.5	1×10^{-6} 5×10^{-7}	2×10^{-5} 8×10^{-7}	0.65 0.50	0.025 0.015	0.060 0.058	0.940 0.942	0.050 0.070	0.020 0.009
Shale 3	1.0	2.5×10^{-6}	4×10^{-6}	0.66	0.020	0.060	0.940	0.055	0.150

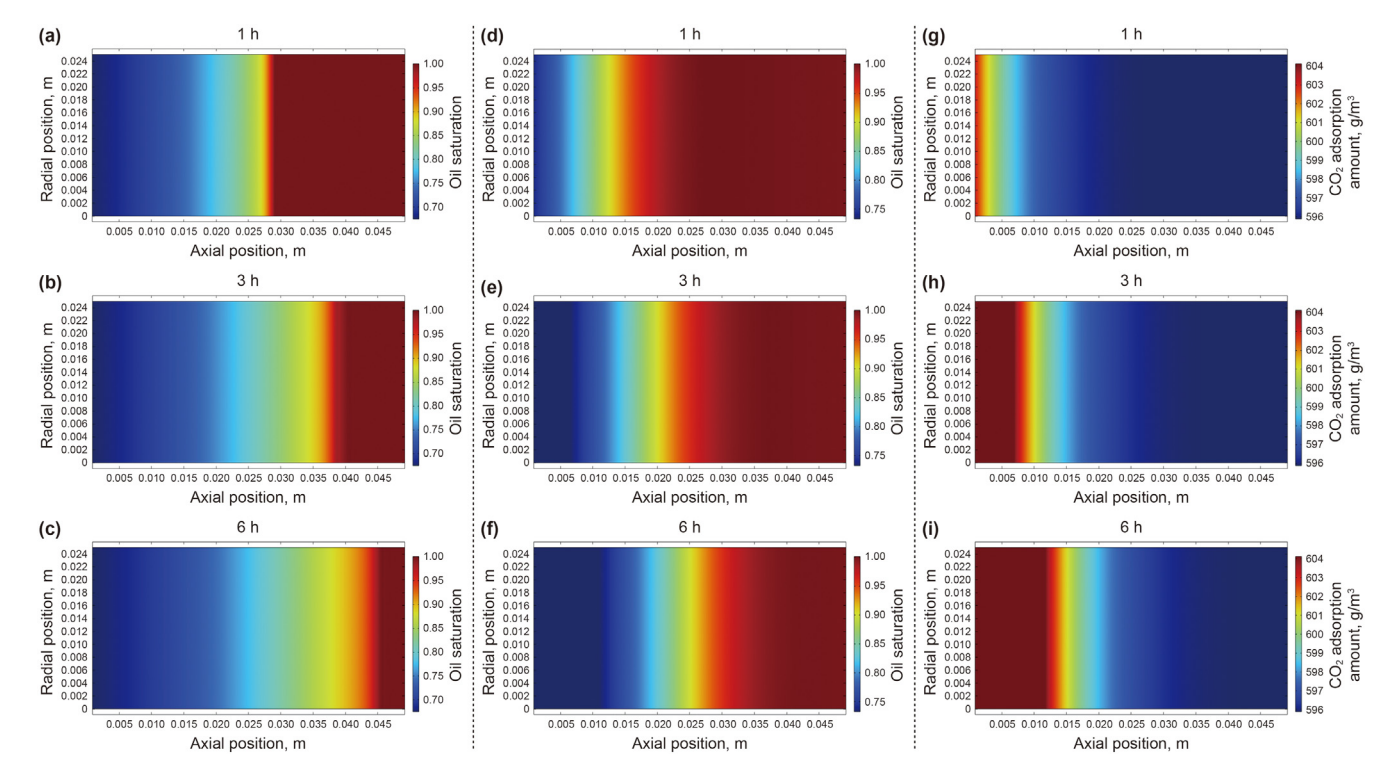
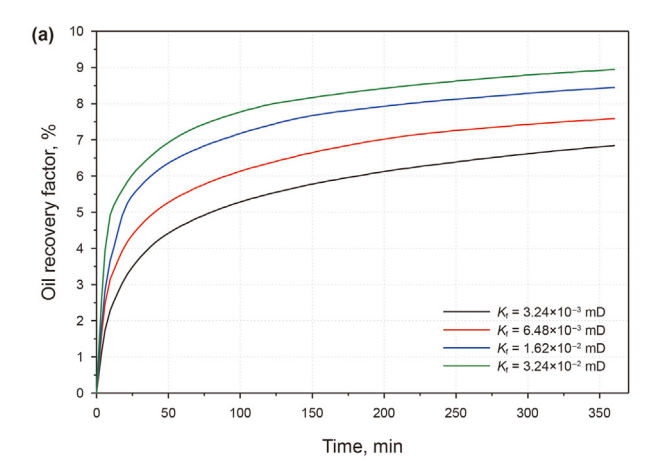
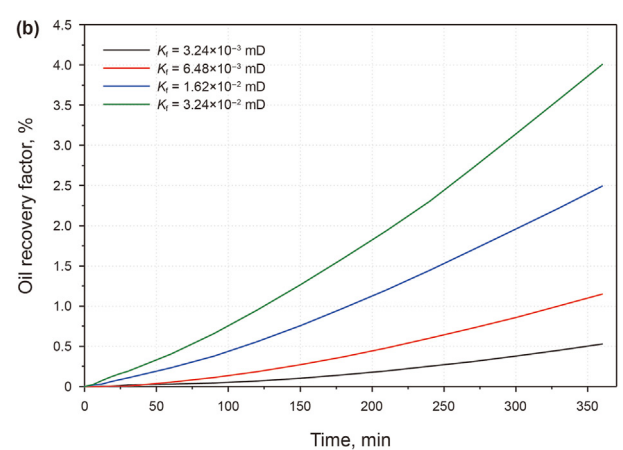


Fig. 11. The dynamic oil saturation of shale bedding fracture system (a, b, c) and shale matrix system (d, e, f), and CO₂ adsorption amount in shale matrix (g, h, i).





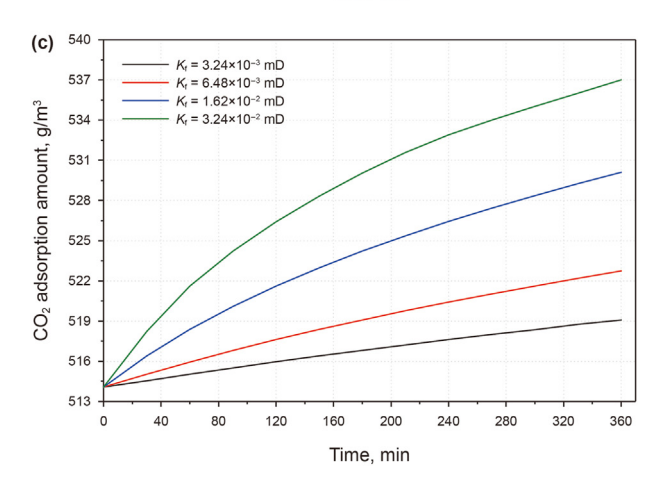


Fig. 12. Effects of the permeability of bedding fracture system on oil recovery factors of bedding fracture system (**a**) and shale matrix system (**b**), and the CO_2 adsorption amount in shale matrix (**c**).

shale matrix and shale bedding fractures that cannot be measured experimentally are derived by fitting the experimental data, as shown in Table 4. The permeability of the shale matrix is found to be 2-3 orders of magnitude lower than that of the shale bedding fracture system. However, the porosity of the shale matrix exceeds that of the bedding fracture system, as it mainly consists of nanopores, providing reservoir space for CO_2 and shale oil due to its high specific surface area (Wei et al., 2016; Hu et al., 2023).

The proposed numerical model highlights the combined mechanisms of molecular diffusion, flow, and adsorption of oil and

 CO_2 phases during $SC-CO_2$ injection in shale oil reservoirs. The distribution of oil saturation and CO_2 adsorption at different time is depicted in Fig. 11. During $SC-CO_2$ injection, the reduction in oil saturation primarily occurs within the shale bedding fractures, suggesting that the bedding fractures play a critical role in both oil storage and production (Fig. 11(a)-(c)). Furthermore, the CO_2 adsorption amount in the shale matrix increases proportionally with the expansion of the CO_2 sweep distance (Fig. 11(g)-(i)).

5. Discussion

In this study, the enhancement of carbon storage capacity and oil recovery potential in shale oil reservoirs are investigated. Three key influencing factors are analyzed, which include the permeability of the shale bedding fracture system, the volume fraction of kerogen and organic pores, and pressure-related parameters including SC-CO₂ injection pressure, production pressure, and the differential pressure between them.

5.1. Effect of the shale bedding fracture permeability

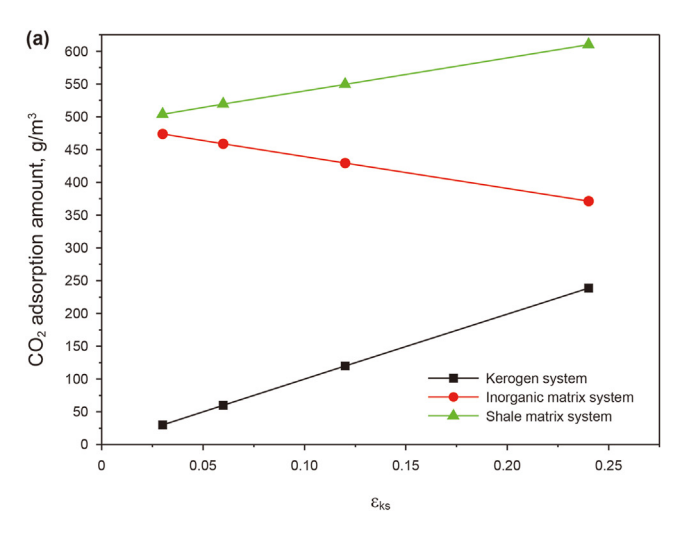
The shale bedding fractures are both storage space and pathways for mass transfer (Sun et al., 2023; He et al., 2024). Four scenarios of bedding fracture permeability (K_f), namely 3.24×10^{-3} (base case), 6.48 \times 10⁻³, 1.62 \times 10⁻², and 3.24 \times 10⁻² mD are simulated to assess the impact on carbon storage capacity and oil recovery efficiency. As shown in Fig. 12(a) and (b), the oil recovery in both the shale bedding fracture system and shale matrix system significantly increases with the enhancement of permeability in the shale bedding fracture system. Specially, when $K_f = 3.24 \times 10^{-3}$ mD (base case), the oil recovery factor of the shale matrix system is 0.99%. This increases to 4.75% with $K_f = 3.24 \times 10^{-2}$ mD, which is nearly four times higher than the base case. Additionally, the shale bedding fracture permeability affects CO₂ adsorption in the shale matrix system. For the scenario $K_f = 3.24 \times 10^{-2}$ mD, the CO₂ adsorption amount is 519.09 g/m³, however, for the scenario $K_{\rm f} = 3.24 \times 10^{-2}$ mD, the CO₂ adsorption amount increases to 537.01 g/m³ (Fig. 12(c)).

5.2. Effects of the volume fraction of kerogen and organic pores

Shale oil reservoirs possess substantial capacity for carbon storage through adsorption in the shale matrix (Kang et al., 2011; Zhao et al., 2021). To investigate the effect of the organic kerogen content on CO₂ adsorption amount in the shale matrix, the volume fraction of the kerogen parameter (ε_{ks}) was adjusted while keeping other parameters constant. Shale oil reservoirs typically contain organic content ranging from 0.5 wt% to approximately 15 wt% (Li et al., 2021). Based on the definition of ε_{ks} in Eq. (43) (Zhang et al., 2021), four scenarios of ε_{ks} , namely 3%, 6% (base case), 12%, and 24% were simulated. As shown in Fig. 13(a), the increase in ε_{ks} significantly improves the CO₂ adsorption amount in the kerogen system and decreases the adsorption amount in the inorganic matrix, leading to a net increase in total adsorption amount in the shale matrix, specifically 503.93, 519.09, 549.40, and 609.88 g/m^3 , respectively. These results indicate that the adsorption of organic kerogen dominates carbon storage in organic-rich shale. This may be due to the higher affinity of kerogen for CO2 compared to clay minerals (eg., illite, smectite), which is influenced by the chemical composition and bonding (Tian et al., 2019).

$$\varepsilon_{\rm ks} = {\rm TOC} \frac{\rho_{\rm rock}}{\rho_{\rm to}} S_{\rm f} \tag{43}$$

where TOC is the total organic content, wt%; $\rho_{\rm rock}$ is the rock



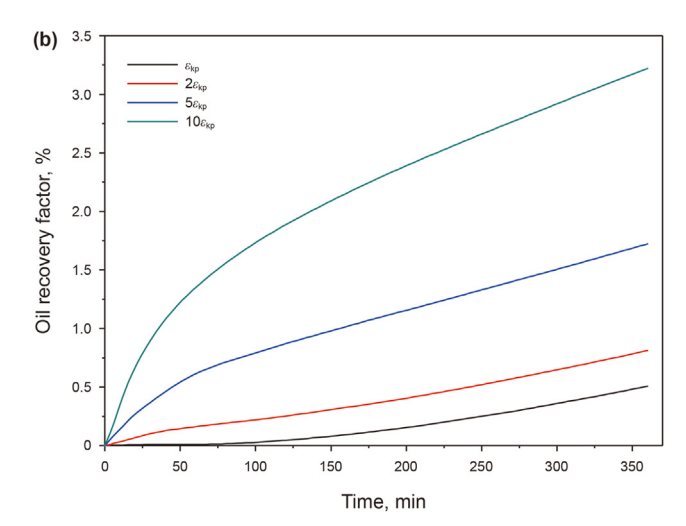


Fig. 13. (a) Effect of the volume fraction of kerogen (ε_{kS}) on CO₂ adsorption amount in shale oil reservoir. (b) Effect of the organic porosity (ε_{kD}) on oil recovery factor.

density, g/cm^3 ; ρ_k is the density of dry kerogen, 1.25 g/cm^3 is selected in this study; and S_f is the swelling factor of kerogen saturated with hydrocarbons, $S_f = 1.3$ in this study (Larsen and Li, 1994; Okiongbo et al., 2005; Ertas et al., 2006).

SC-CO₂ is an ideal solvent for extracting oil from kerogen (Tucker et al., 2000). Hydrocarbons in kerogen can be replaced by CO₂ when the mole fraction of CO₂ in the oil—CO₂ mixture exceeds a threshold value, leading to the displacement of hydrocarbons by CO₂, and thus enhancing oil recovery in shale oil reservoirs (Zhu et al., 2018a; Zhao et al., 2021). The simulation results under four different volume fractions of organic pores ($\varepsilon_{\rm kp}$) are illustrated in Fig. 13(b). The results demonstrate that oil recovery factors in the matrix system significantly increase with the elevation of $\varepsilon_{\rm kp}$. An enhancement of $\varepsilon_{\rm kp}$, ranging from 0.025 to 0.25, results in a significant increase in the oil recovery factor of the shale matrix, increasing from 7.33% to 10.03%.

5.3. Effects of the pressure-related parameters

The pressure-related parameters examined in this study include SC-CO₂ injection pressure in inlet, production pressure in outlet, and the differential pressure between the injection pressure and the production pressure, which is referred to differential pressure in the following text. The effects of these parameters on carbon storage and shale oil recovery factor were analyzed by varying the injection and production pressures for the same sample. The numerical simulation results are presented in Fig. 14. As shown in Fig. 14(a) and (b), when the differential pressure is 5 MPa, the recovery factors for shale bedding fractures and the matrix systems are significantly higher compared to when the pressure difference is 3 MPa. Additionally, at a differential pressure of 3 MPa, the recovery factors are notably higher than those observed at 1 MPa. These results indicate that as the differential pressure increases, the recovery factors for shale bedding fractures and the matrix systems exhibit an upward trend.

Production pressure has a significant impact on the CO_2 adsorption amount in the shale matrix, as shown in Fig. 14(c). It demonstrates that as the production pressure increases from 8 to 10 MPa, the CO_2 adsorption amount significantly increases. And under the same production pressure, an increase in injection pressure results in a higher CO_2 adsorption capacity. For instance, when the production pressure is constant at 8 MPa, the adsorption amount of CO_2 increased only by 4.51 and 8.39 g/m³, respectively, when the injection pressure was adjusted from 9 to 11 MPa and

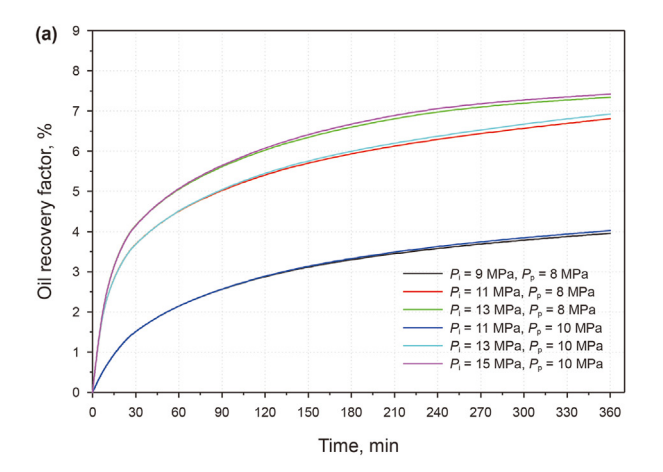
13 MPa. Therefore, the simulation results suggest that injection pressure and pressure gradient have a relatively minor impact on CO₂ adsorption in Fig. 14(c).

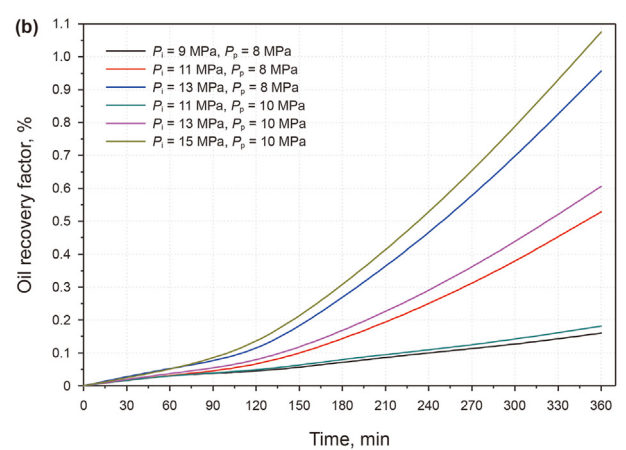
In conclusion, the differential pressure is a key factor influencing the oil recovery factor. Before gas breakthrough occurs, a high differential pressure leads to a higher total oil recovery factor. To achieve higher ${\rm CO}_2$ adsorption amounts in shale oil reservoirs, establishing high production pressure is essential. This indicates that both high production and injection pressures are necessary to maintain high differential pressure values, which are vital for maximizing carbon storage capacity and oil recovery efficiency.

6. Conclusions

In this study, a series of CO₂ injection experiments were conducted to simulate carbon storage and enhanced oil recovery, aiming to validate the feasibility of carbon storage and oil recovery in shale oil reservoirs with natural fractures. A multiscalemultiphase numerical model was developed to capture the complex interactions within the reservoir. The full-scale pore systems, encompassing the kerogen system, inorganic matrix system, and shale bedding fracture system were defined as triple-continuum media in the model. The model integrated the mechanisms of molecular diffusion, adsorption, and viscous flow of oil and CO2 phases to accurately represent the mass transfer processes. The finite element method was used to numerically solve these partial differential equations and the solutions were validated against experimental results. Based on both experimental data and numerical simulations, key properties governing multiscale and multiphase mass transfer during CO₂ injection were analyzed, leading to the following conclusions:

- (1) The nanoscale pores are the primary reservoir spaces for both shale oil and CO₂ in shale oil reservoirs. The comparison of gaseous CO₂ and supercritical CO₂ injection experiments indicates that SC-CO₂ can significantly enhance oil recovery and concurrently storage in shale matrix.
- (2) Shale bedding fractures are the reservoir space for shale oil and the key channels for mass transfer during CO₂ injection. The numerical simulation results have showed that increasing the permeability of the bedding fracture system causes a significant improvement in oil recovery factor and CO₂ adsorption amount.





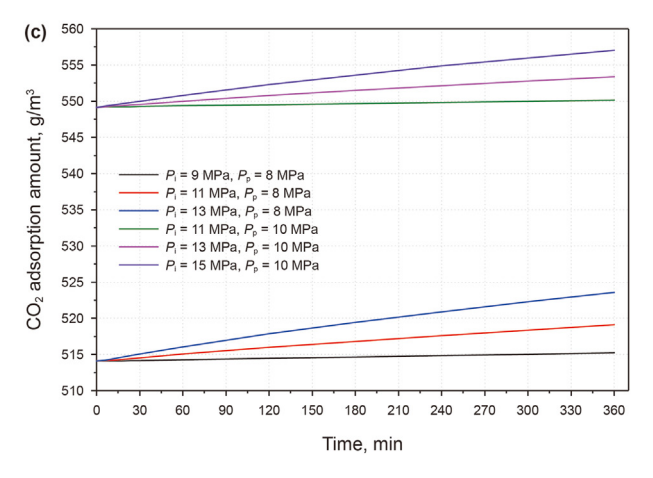


Fig. 14. Effects of pressure on oil recovery factors of the shale matrix system (**a**) and bedding fracture system (**b**), and the CO_2 adsorption amount in the shale matrix system (**c**). Notes: P_1 is the injection pressure in the inlet, and P_p is the production pressure in the outlet.

- (3) Organic kerogen has a significant impact on carbon storage and oil recovery efficiency in the shale matrix. An increase in kerogen content enhances CO₂ adsorption capacity, and the oil recovery efficiency improves with higher organic porosity.
- (4) CO₂ adsorption capacity significantly enhances with the increase in the production pressure. The higher injection pressure can lead to higher recovery factors under the same production pressure. High injection pressure and high

production pressure are critical factors for improving simultaneously CO₂ storage and shale oil recovery.

CRediT authorship contribution statement

Lu Wang: Writing — original draft, Methodology, Investigation, Data curation, Conceptualization. **Gang Wu:** Validation, Methodology, Investigation, Data curation. **Meng Lu:** Project administration, Investigation, Conceptualization. **Xiao-Fei Fu:** Project administration, Data curation. **Jun Feng:** Validation, Supervision. **Zhe-Jun Pan:** Writing — review & editing, Supervision, Resources, Conceptualization.

Declaration of competing interest

The authors declare that there is no conflict of interest.

Acknowledgments

This work was supported by the Key Project of National Natural Science Foundation of China (U23A20596).

References

Aljamaan, H., Holmes, R., Vishal, V., Haghpanah, R., Wilcox, J., Kovscek, A.R., 2017. CO₂ storage and flow capacity measurements on idealized shales from dynamic breakthrough experiments. Energy Fuels 31 (2), 1193–1207. https://doi.org/ 10.1021//acs.energyfuels.6b02286.

Bouzgarrou, S., Jadli, H., Stiti, N., Hamdi, N., Slimi, K., Bagane, M., 2015. Experimental adsorption and modelisation of CO₂ on adsorbents collected from Elborma Field in South Tunisia. J. Surface Eng. Mater. Adv. Technol 5 (1), 52–63. https://doi.org/10.4236/jsemat.2015.51006.

Cao, G., Lin, M., Ji, L., Jiang, W., Yang, M., 2019. Characterization of pore structures and gas transport characteristics of Longmaxi shale. Fuel 258 (15), 116146. https://doi.org/10.1016/j.fuel.2019.116146.

Cao, P., Liu, J., Leong, Y.K., 2017. A multiscale-multiphase simulation model for the evaluation of shale gas recovery coupled the effect of water flowback. Fuel 199 (1), 191–205. https://doi.org/10.1016/j.fuel.2017.02.078.

Chouikhi, N., Cecilia, J.A., Vilarrasa García, E., Besghaier, S., Chlendi, M., Franco Duro, F.I., Rodriguez Castellon, E., Bagane, M., 2019. CO₂ adsorption of materials synthesized from clay minerals: a review. Minerals 9 (9), 514. https://doi.org/10.3390/min9090514.

Du, F., Nojabaei, B., 2020. Estimating diffusion coefficients of shale oil, gas, and condensate with nano-confinement effect. J. Petrol. Sci. Eng. 193, 107362. https://doi.org/10.1016/j.petrol.2020.107362.

Ertas, D., Kelemen, S.R., Halsey, T.C., 2006. Petroleum expulsion Part 1. Theory of kerogen swelling in multicomponent solvents. Energy Fuels 20 (1), 295–300. https://doi.org/10.1021/efef058024k.

Fakher, S., Imqam, A., 2019. A review of carbon dioxide adsorption to unconventional shale rocks methodology, measurement, and calculation. Discover Appl. Sci. 2, 5. https://doi.org/10.1007/s42452-019-1810-8.

Falk, K., Pellenq, R., Ulm, F.J., Coasne, B., 2015. Effect of chain length and pore accessibility on alkane adsorption in kerogen. Energy Fuels 29 (12), 7889–7896. https://doi.org/10.1021/acs.energyfuels.5b02015.

Fernø, M.A., Hauge, L.P., Rognmo, A.U., Gauteplass, J., Graue, A., 2015. Flow visualization of CO₂ in tight shale formations at reservoir conditions. Geophys. Res. Lett. 42 (18), 7414–7419. https://doi.org/10.1002/2015GL065100.

Fu, C., Du, Y., Song, W., Sang, S., Pan, Z., Wang, N., 2023. Application of automated mineralogy in petroleum geology and development and CO₂ sequestration: a review. Mar. Petrol. Geol. 151, 106206. https://doi.org/10.1016/ i.marpetgeo.2023.106206.

Fu, C., Xu, X., Du, Y., Kou, X., 2024. Experimental study on the influence of pore structure on spontaneous imbibition in marine black shale. Capillarity 10 (3), 57–72. https://doi.org/10.46690/capi.2024.03.01.

Gao, Y., Wang, M., Li, Y., Jiang, Z., Deng, Y., Qin, J., 2023. Multi-scale pore structure characterization of lacustrine fine-grained mixed sedimentary rocks and its controlling factors: a case study of Lucaogou Formation in Jimusar Sag. Energy Fuels 37 (2), 977–992. https://doi.org/10.1021/acs.energyfuels.2c03411.

Ge, X., Myers, M.T., Liu, J., Fan, Y., Zahid, M.A., Zhao, J., Hathon, L., 2021. Determining the transverse surface relaxivity of reservoir rocks: a critical review and perspective. Mar. Petrol. Geol. 126, 104934. https://doi.org/10.1016/ j.marpetgeo.2021.104934.

Gou, Q., Xu, S., Hao, F., Yang, F., Zhang, B., Shu, Z., Zhang, A., Wang, Y., Lu, Y., Cheng, X., Qing, J., Gao, M., 2019. Full-scale pores and micro-fractures characterization using FE-SEM, gas adsorption, nano-CT and micro-CT: a case study of the Silurian Longmaxi Formation shale in the Fuling area, Sichuan Basin, China.

- Fuel 253 (1), 167-179. https://doi.org/10.1016/j.fuel.2019.04.116.
- Guo, B.E., Xiao, N., Martyushev, D., Zhao, Z., 2024. Deep learning-based pore network generation: numerical insights into pore geometry effects on microstructural fluid flow behaviors of unconventional resources. Energy 294 (1), 130990. https://doi.org/10.1016/j.energy.2024.130990.
- Hazra, B., Vishal, V., Sethi, C., Chandra, D., 2022. Impact of supercritical CO₂ on shale reservoirs and its implication for CO₂ sequestration. Energy Fuels 36 (17), 9882–9903. https://doi.org/10.1021/acs.energyfuels.2c01894.
- He, W., Zhao, Y., Zhong, J., Sun, N., 2024. Characteristics and significance of micron pores and micron fractures in shale oil reservoirs of cretaceous qingshankou formation in Gulong sag, Songliao Basin. Lithol. Reservoir. 36 (3), 1–18. https://doi.org/10.12108/yxyqc.20240301 in Chinese.
- Hu, H., Zhang, T., Wiggins Camacho, J.D., Ellis, G.S., Lewan, M.D., Zhang, X., 2015. Experimental investigation of changes in methane adsorption of bitumen-free Woodford shale with thermal maturation induced by hydrous pyrolysis. Mar. Petrol. Geol. 59, 114–128. https://doi.org/10.1016/j.marpetgeo.2014.07.029.
- Hu, R., Wang, C., Zhang, M., Zhang, Y., Zhao, J., 2023. The study of multi-scale specific surface area in shale rock with fracture-micropore-nanopore. Processes 11 (4), 1015. https://doi.org/10.3390/pr11041015.
- Huang, L., Ning, Z., Wang, Q., Qi, R., Zeng, Y., Qin, H., Ye, H., Zhang, W., 2018. Molecular simulation of adsorption behaviors of methane, carbon dioxide and their mixtures on kerogen: effect of kerogen maturity and moisture content. Fuel 211, 159–172. https://doi.org/10.1016/j.fuel.2017.09.060.
- Javadpour, F., Fisher, D., Unsworth, M., 2007. Nanoscale gas flow in shale gas sediments. J. Can. Petrol. Technol. 46 (10). https://doi.org/10.2118/07-10-06.
- Jia, B., Chen, Z., Xian, C., 2022. Investigations of CO₂ storage capacity and flow behavior in shale formation. J. Petrol. Sci. Eng. 208, 109659. https://doi.org/ 10.1016/j.petrol.2021.109659.
- Jia, B., Tsau, J.S., Barati, R., 2019. A review of the current progress of CO₂ injection EOR and carbon storage in shale oil reservoirs. Fuel 236 (15), 404–427. https://doi.org/10.1016/j.fuel.2018.08.103.
- Jin, L., Hawthorne, S., Sorensen, J., Pekot, L., Kurz, B., Smith, S., Heebink, L., Herdegen, V., Bosshart, N., Torres, J., Dalkhaa, C., Peterson, K., Gorecki, C., Steadman, E., Harju, J., 2017. Advancing CO₂ enhanced oil recovery and storage in unconventional oil play—experimental studies on Bakken shales. Appl. Energy 208 (15), 171–183. https://doi.org/10.1016/j.apenergy.2017.10.054.
- Kang, S.M., Fathi, E., Ambrose, R.J., Akkutlu, I.Y., Sigal, R.F., 2011. Carbon dioxide storage capacity of organic-rich shales. SPE J. 16 (4), 842–855. https://doi.org/ 10.2118/134583-PA.
- Kazemi, H., Merrill, L.S., Porterfield, K.L., Zeman, P.R., 1976. Numerical simulation of water-oil flow in naturally fractured reservoirs. Soc. Petrol. Eng. J. 16 (6), 317–326. https://doi.org/10.2118/5719-PA.
- Kleinberg, R., Horsfield, M., 1990. Transverse relaxation processes in porous sedimentary rock. J. Magn. Reson. 88 (1), 9–19. https://doi.org/10.1016/0022-2364(90)90104-H.
- Langmuir, I., 1918. The adsorption of gases on plane surfaces of glass, mica and platinum. J. Am. Chem. Soc. 40 (9), 1361–1403. https://doi.org/10.1021/ IA02242A004.
- Larsen, J.W., Li, S., 1994. Solvent swelling studies of Green River kerogen. Energy Fuels 8, 932–936. https://doi.org/10.1021/ef00046a017.
- Lashgari, H.R., Sun, A., Zhang, T., Pope, G.A., Lake, L.W., 2019. Evaluation of carbon dioxide storage and miscible gas EOR in shale oil reservoirs. Fuel 241, 1223–1235. https://doi.org/10.1016/j.fuel.2018.11.076.
- Li, L., Zhang, Y., Sheng, J.J., 2017. Effect of the injection pressure on enhancing oil recovery in shale cores during the CO₂ huff-n-puff process when it is above and below the minimum miscibility pressure. Energy Fuels 31 (4), 3856–3867. https://doi.org/10.1021/acs.energyfuels.7b00031.
- Li, W., Zhang, M., Nan, Y., Pang, W., Jin, Z., 2021. Molecular dynamics study on CO₂ storage in water-filled kerogen nanopores in shale reservoirs: effects of kerogen maturity and pore size. Langmuir 37 (1), 542–552. https://doi.org/10.1021/acs.langmuir.0c03232.
- Liu, Q., Sun, M., Sun, X., Liu, B., Ostadhassan, M., Huang, W., Chen, X., Pan, Z., 2023. Pore network characterization of shale reservoirs through state-of-the-art X-ray computed tomography: a review. Gas Sci. Eng. 113, 204967. https://doi.org/10.1016/j.jgsce.2023.204967.
- Liu, Y., Wilcox, J., 2012. Effects of surface heterogeneity on the adsorption of CO₂ in microporous carbons. Environ. Sci. Technol. 46 (3), 1940–1947. https://doi.org/ 10.1021/es204071g.
- Liu, Y., Yao, Y., Liu, D., Zhang, C., 2023. Nuclear magnetic resonance investigation of forced imbibitions in Longmaxi shales: consideration of different boundary conditions. Energy Fuels 37 (8), 5853–5866. https://doi.org/10.1021/ acs.energyfuels.3c00404.
- Luo, Y., Zheng, T., Xiao, H., Liu, X., Zhang, H., Wu, Z., Zhao, X., Xia, D., 2022. Identification of distinctions of immiscible CO₂ huff and puff performance in Chang 7 tight sandstone oil reservoir by applying NMR, microscope and reservoir simulation. J. Petrol. Sci. Eng. 209, 109719. https://doi.org/10.1016/j.petrol.2021.00719
- Lv, W., Gong, H., Dong, M., Li, Y., Sun, H., Sun, Z., Jiang, H., 2024. Potential of nonionic polyether surfactant-assisted CO₂ huff-n-puff for enhanced oil recovery and CO₂ storage in ultra-low permeability unconventional reservoirs. Fuel 359, 130474. https://doi.org/10.1016/j.fuel.2023.130474.
- Martyushev, D.A., Davoodi, S., Kadkhodaie, A., Riazi, M., Kazemzadeh, Y., Ma, T., 2024. Multiscale and diverse spatial heterogeneity analysis of void structures in reef carbonate reservoirs. Geoenergy Sci. Eng. 233, 212569. https://doi.org/10.1016/j.geoen.2023.212569.

Martyushev, D.A., Ponomareva, I.N., Filippov, E.V., 2023. Studying the direction of hydraulic fracture in carbonate reservoirs: using machine learning to determine reservoir pressure. Petrol. Res. 8 (2), 226–233. https://doi.org/10.1016/i.ptfrs.2022.06.003.

- Mohammed, S., Gadikota, G., 2019. CO₂-induced displacement and diffusive transport of shale geofluids in silica nanopores of varying sizes. J. CO₂ Util. 32 (1), 37–45. https://doi.org/10.1016/j.jcou.2019.03.023.
- Okiongbo, K.S., Aplin, A.C., Larter, S., 2005. Changes in type II kerogen density as a function of maturity: evidence from the Kimmeridge clay formation. Energy Fuels 19 (6), 2495–2499. https://doi.org/10.1021/ef050194+.
- Pan, Z., Connell, L.D., Camilleri, M., 2010. Laboratory characterisation of coal reservoir permeability for primary and enhanced coalbed methane recovery. Int. J. Coal Geol. 82 (3–4), 252–261. https://doi.org/10.1016/j.coal.2009.10.019.
- Reichenberger, V., Jakobs, H., Bastian, P., Helmig, R., 2006. A mixed-dimensional finite volume method for two-phase flow in fractured porous media. Adv. Water Resour. 29 (7), 1020–1036. https://doi.org/10.1016/i.advwatres.2005.09.001.
- Sang, Q., 2018. Determination of organic and inorganic hydrocarbon saturations and effective porosities in shale using vacuum-imbibition method. Int. J. Coal Geol. 200, 123–124. https://doi.org/10.1016/j.coal.2018.10.010.
- Sui, H., Zhang, F., Zhang, L., Wang, Z., Yuan, S., Wang, D., Wang, Y., 2023. Mechanism of CO₂ enhanced oil recovery in kerogen pores and CO₂ sequestration in shale: a molecular dynamics simulation study. Fuel 349, 128692. https://doi.org/10.1016/i.fuel.2023.128692.
- Sun, L., He, W., Feng, Z., Zeng, H., Jiang, H., Pan, Z., 2022. Shale oil and gas generation process and pore fracture system evolution mechanisms of the continental Gulong shale, Songliao Basin, China. Energy Fuels 36 (13), 6893–6905. https:// doi.org/10.1021/acs.energyfuels.2c01407.
- Sun, L., Wang, X., Feng, Z., Shao, H., Zeng, H., Jiang, H., 2023. Formation mechanisms of nano-scale pores/fissures and shale oil enrichment characteristics for Gulong shale, Songliao Basin. Oil Gas Geol 44 (6), 1350–1365. https://doi.org/10.11743/ogg20230602 (in Chinese).
- Tian, H., He, K., Huangfu, Y., Liao, F., Wang, X., Zhang, S., 2024. Oil content and mobility in a shale reservoir in Songliao Basin, Northeast China: insights from combined solvent extraction and NMR methods. Fuel 357, 129678. https:// doi.org/10.1016/j.fuel.2023.129678.
- Tian, S., Bai, R., Dai, X., Lu, Y., Chen, Jie, Wang, G., 2022. Experimental study on the adsorption properties of methane and carbon dioxide in illite, montmorillonite and calcite. J. Petrol. Sci. Eng. 219, 111144. https://doi.org/10.1016/ i.petrol.2022.111144.
- Tian, S., Wang, T., Li, G., Sheng, M., Zhang, P., 2019. Nanoscale surface properties of organic matter and clay minerals in shale. Langmuir 35 (17), 5711–5718. https://doi.org/10.1021/acs.langmuir.9b00157.
- Tucker, J.D., Masri, B.A., Lee, S., 2000. A comparison of retorting and supercritical extraction techniques on El-Lajjun oil shale. Energy Sources 22 (5), 453–463. https://doi.org/10.1080/00908310050013866.
- Wang, L., Du, Y., Wu, G., Fu, X., Xu, C., Pan, Z., 2025. Application of nuclear magnetic resonance technology in reservoir characterization and CO₂ enhanced recovery for shale oil: a review. Mar. Petrol. Geol. 177, 107353. https://doi.org/10.1016/j.marpetgeo.2025.107353.
- Wang, L., Zhang, Y., Zou, Rui, Zou, Run, Huang, L., Liu, Y., Meng, Z., Wang, Z., Lei, H., 2023. A systematic review of CO₂ injection for enhanced oil recovery and carbon storage in shale reservoirs. Int. J. Hydrogen Energy 48 (95), 37134–37165. https://doi.org/10.1016/j.ijhydene.2023.06.099.
- Warren, J.E., Root, P.J., 1963. The behavior of naturally fractured reservoirs. Soc. Petrol. Eng. J. 3 (3), 245–255. https://doi.org/10.2118/426-PA.
- Wei, M., Zhang, L., Xiong, Y., Li, J., Peng, P., 2016. Nanopore structure characterization for organic-rich shale using the non-local-density functional theory by a combination of N₂ and CO₂ adsorption. Microporous Mesoporous Mater. 227, 88–94. https://doi.org/10.1016/j.micromeso.2016.02.050.
- Xie, W., Wang, M., Wang, H., 2021. Adsorption characteristics of CH₄ and CO₂ in shale at high pressure and temperature. ACS Omega 6 (28), 18527–18536. https://doi.org/10.1021/acsomega.1c02921.
- Xu, H., Wang, F., Liu, Y., Meng, X., Liu, L., 2024. Mechanism study on the influence of wettability on CO₂ displacement of shale oil in nanopores. Fuel 376, 132695. https://doi.org/10.1016/j.fuel.2024.132695.
- Yan, B., Wang, Y., Killough, J.E., 2016. Beyond dual-porosity modeling for the simulation of complex flow mechanisms in shale reservoirs. Comput. Geosci. 20, 69–91. https://doi.org/10.1007/s10596-015-9548-x.
- Yang, Z., Wang, W., Dong, M., Wang, J., Li, Y., Gong, H., Sang, Q., 2016. A model of dynamic adsorption—diffusion for modeling gas transport and storage in shale. Fuel 173, 115—128. https://doi.org/10.1016/j.fuel.2016.01.037.
- Yao, Y., Liu, D., Che, Y., Tang, D., Tang, S., Huang, W., 2010. Petrophysical characterization of coals by low-field nuclear magnetic resonance (NMR). Fuel 89 (7), 1371–1380. https://doi.org/10.1016/j.fuel.2009.11.005.
- Zhang, M., Yao, J., Sun, H., Zhao, J., Fan, D., Huang, Z., Wang, Y., 2015. Triple-continuum modeling of shale gas reservoirs considering the effect of kerogen. J. Nat. Gas Sci. Eng. 24, 252—263. https://doi.org/10.1016/j.jngse.2015.03.032.
- Zhang, R., Wu, J., Zhao, Y., He, X., Wang, R., 2021. Numerical simulation of the feasibility of supercritical CO₂ storage and enhanced shale gas recovery considering complex fracture networks. J. Petrol. Sci. Eng. 204, 108671. https:// doi.org/10.1016/j.petrol.2021.108671.
- Zhang, S., Jia, B., Zhao, J., Pu, H., 2021. A diffuse layer model for hydrocarbon mass transfer between pores and organic matter for supercritical CO₂ injection and sequestration in shale. Chem. Eng. J. 406, 126746. https://doi.org/10.1016/

j.cej.2020.126746.

- Zhao, R., Xue, H., Lu, S., Li, J., Tian, S., Wang, M., Dong, Z., 2022. Multi-scale pore structure characterization of lacustrine shale and its coupling relationship with material composition: an integrated study of multiple experiments. Mar. Petrol. Geol. 140, 105648. https://doi.org/10.1016/j.marpetgeo.2022.105648.
- Zhao, X., Sang, Q., Li, Y., Liu, H., Dong, M., 2021. CO₂-kerogen interaction dominated CO₂-oil counter-current diffusion and its effect on ad-/absorbed oil recovery and CO₂ sequestration in shale. Fuel 294, 120500. https://doi.org/10.1016/i.fuel.2021.120500.
- Zhao, Z., Shou, Y., Zhou, X., 2023. Microscopic cracking behaviors of rocks under uniaxial compression with microscopic multiphase heterogeneity by deep learning. Int. J. Min. Sci. Technol. 33 (4), 411–422. https://doi.org/10.1016/ j.ijmst.2022.12.008.
- Zhao, Z., Shou, Y.D., Zhou, X.P., 2024. A novel digital extraction approach of pore network models from carbonates inspired by quantum genetic optimization techniques. Acta Geotechnica 19, 3805–3820. https://doi.org/10.1007/s11440-

024-02310-2.

- Zhao, Z., Zhou, X.P., 2024. Digital microscopic multiphase heterogeneity representation and its effects on micromechanics and cracking behaviors of geomaterials. Rock Mech. Rock Eng. 57, 7443–7459. https://doi.org/10.1007/s00603-024-03905-7.
- Zhu, C., Li, Y., Gong, H., Sang, Q., Li, Z., Dong, M., 2018a. Adsorption and dissolution behaviors of carbon dioxide and n-dodecane mixtures in shale. Energy Fuels 32 (2), 1374–1386. https://doi.org/10.1021/acs.energyfuels.7b03417.
- Zhu, C., Li, Y., Zhao, Q., Gong, H., Sang, Q., Zou, H., Dong, M., 2018b. Experimental study and simulation of CO₂ transfer processes in shale oil reservoir. Int. J. Coal Geol. 191, 24–36. https://doi.org/10.1016/j.coal.2018.03.002.
- Zhu, C., Qin, X., Li, Y., Gong, H., Li, Z., Xu, L., Dong, M., 2019. Adsorption and dissolution behaviors of CO₂ and n-alkane mixtures in shale: effects of the alkane type, shale properties and temperature. Fuel 253, 1361–1370. https://doi.org/10.1016/j.fuel.2019.05.002.